IMPACT OF HALOS ON THE SIMULATED COSMIC DAWN 21-CM SIGNAL

M.Sc. Thesis

By:
Vednarayan Iyer

DEPARTMENT OF ASTRONOMY , ASTROPHYSICS AND SPACE ENGINEERING

INDIAN INSTITUTE OF TECHNOLOGY INDORE

April, 2023

IMPACT OF HALOS ON THE SIMULATED COSMIC DAWN 21-CM SIGNAL

A THESIS

Submitted in partial fulfillment of the requirements for the award of the degree
of
Master of Science

by
Vednarayan Iyer

DEPARTMENT OF ASTRONOMY , ASTROPHYSICS AND SPACE ENGINEERING

INDIAN INSTITUTE OF TECHNOLOGY INDORE

April, 2023

INDIAN INSTITUTE OF TECHNOLOGY INDORE

CANDIDATE'S DECLARATION

I hereby certify that the work which is being presented in the thesis entitled **"Impact of halos on the simulated cosmic dawn 21-cm signal"** in the partial fulfillment of the requirements for the award of the degree of MASTER OF SCIENCE and submitted in the DEPARTMENT OF ASTRONOMY , ASTROPHYSICS AND SPACE ENGINEERING , Indian Institute of Technology Indore, is an authentic record of my own work carried out during the time period from July, 2022 to May, 2023 under the supervision of Dr. Suman Majumdar . The matter presented in this thesis has not been submitted by me for the award of any other degree of this or any other institute.

Ved Iyer
03/05/2023

Signature with date
(Vednarayan Iyer)

This is to certify that the above statement made by the candidate is correct to the best of my knowledge.

Suman Majumdar
03/05/2023

Signature of the Supervisor of
M.Sc. Thesis
(DR.SUMAN MAJUMDAR)

Vednarayan Iyer has successfully given his M.Sc. Oral Examination held on ..24/04/2023..

Suman Majumdar
03/05/2023

Signature(s) of Supervisor(s) of
MSc thesis, Date:

S. Das

Convener, DPGC
Date:- 02/06/2023

Manoneeta Chakraborty

Signature of PSPC Member 1
Date:- 03/05/2023

Signature of PSPC Member 2
Date:- 03/05/2023

Subhendu Rakshit

Signature of PSPC Member 3
Date:- 03/05/2023

Manoneeta Chakraborty

Signature of HoD (Officiating)
Date:- 06/06/2023

Signature of M.Sc. Co-ordinator
Date:- 03/05/2023

Abstract

Cosmic Dawn (CD) and Epoch of Reionization (EoR) has eluded the observations so far, but with the future Square Kilometer Array (SKA) radio interferometer this will no longer be the case. The 21-cm line, with low excitation energy and low optical depth, is the best candidate to probe this era. There are lots of astrophysical processes taking place in the IGM during this period which will be imprinted on the fluctuations of 21cm brightness temperature. To interpret these fluctuations, one needs an accurate model of the 21cm signal that can be used to constrain the CD-EoR parameters. The publicly available simulations lack the accuracy that will be demanded by the upcoming high-resolution observations. The objective of this thesis project is to improve these simulations by understanding the approximations undertaken by them and then finding an efficient algorithm to incorporate all the astrophysical processes without making the simulation computationally heavy. We have incorporated X-ray heating on top of the existing ReionYuga simulation and initial results show a computationally efficient way to model this process. We have also conducted preliminary statistical analysis on the impact of using halos to calculate the photon flux fied. The end goal is to build a semi-numeric simulation that can be used to constrain the CD-EoR parameters by performing fourier domain (power spectrum, bispectrum) or real space (Largest cluster statistics, Minkowski functions) statistical analysis.

Signature of M.Sc. Co-ordinator
Date:-

Contents

List of Figures

Chapter 1

Introduction

Out of the three eras which are largely unknown to us, the dark ages, cosmic dawn and EoR, the last two eras will soon be observed by the upcoming Square Kilometer Array (SKA). The redshift range to which the cosmic dawn belongs is around z = 30 to z = 6. The latter part of this redshift range from about z = 15 to 6 can potentially be observed by JWST but the sources are rare during this redshift range. This has posed a huge challenge to constrain cosmological parameters from cosmic dawn. Even if the sources are rare, there is a huge amount of neutral hydrogen present in this redshift range and hence any line emission from it will be abundant as well even if the probability of that emission is negligible.

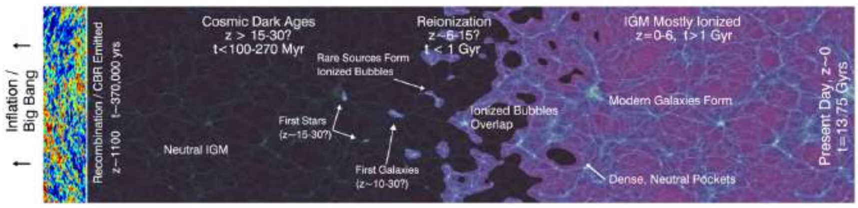

Figure 1.1: Cosmic History (Robertson et al. (2010))

The Lyman-α transition has a high Einstein-A coefficient of 4.7×10^8 so one may hope to use it as probe to trace this period, but it has several major disadvantages for studying the high-z universe like

- High Gunn-Peterson optical depth, a small neutral fraction of order 10^{-3} is enough to render the IGM opaque.
- UV band wavelength, bright UV sources are required to observe, which are scarce at high redshift observing it requires bright UV sources that are very rare at high redshifts.
- High excitation energy, temperature are lower than required to collisionally excite this line during pre-reionization era.

On the contrary, the spin-flip 21-cm line is very weak leading to an effective IGM optical depth of order 1% only, thereby making the entire neutral IGM transparent during the cosmic dawn. Moreover since the excitation energy is low, it can be collisionally excited by the IGM temperature during the redshift of interest. The 21cm line emission from hydrogen is thus the best candidate to probe the cosmic dawn.

1.1 Cosmic Dawn and Epoch of Reionization

The epoch of reionization (EoR) is the time when hydrogen atoms in the Universe were re-ionized as a result of the first stars' radiation. According to the hot Big Bang model, hydrogen atoms formed for the first time during the recombination epoch, as evidenced by the Cosmic Microwave Background (CMB). Following the recombination epoch, the Universe entered a period known as the "dark ages," during which no radiation sources (stars or active galaxies) existed (Fig. 1.1). Throughout this phase, the hydrogen remained largely neutral. Small inhomogeneities in the dark matter density field that existed during the recombination epoch began to grow as a consequence of gravitational instability, leading to the formation of the first stars within galaxies. The dark ages ended when these stars formed, and the "cosmic dawn" began. The first population of luminous stars, and possibly some early population of accreting black holes (quasars), produced ultraviolet (UV) radiation, which ionised hydrogen atoms in the intergalactic medium (IGM).This is referred to as "reionization." This is the universe's second major change in the ionisation state of hydrogen (the first being the recombination).

Reionization began around the time the first structure was formed. The precise details of the star are unknown, but it is most likely in the z *approx* 20-30 range. Looking at the big picture, the reionization process is fairly simple. All of the sources emit radiation, which causes ionised bubbles to form around them. These bubbles continue to grow over time, eventually overlapping and percolating into the IGM. Observations suggest that the end of reionization occurs around z $\approx$ 5-6, at which point the majority of hydrogen returns to being ionised.

The formation of first structures and luminous sources has a direct impact on the process of reionization, which also influences the formation of subsequent structures, making it a crucial component in the study of structure formation. According to observations, the reionization era is a stage of the universe that has not yet been explored; earlier stages (z $\approx$ 1000) have been explored by the CMB, whereas the post-reionization stage (z *approx* 6) has been explored by a variety of observations based on UV galaxies, quasars, and

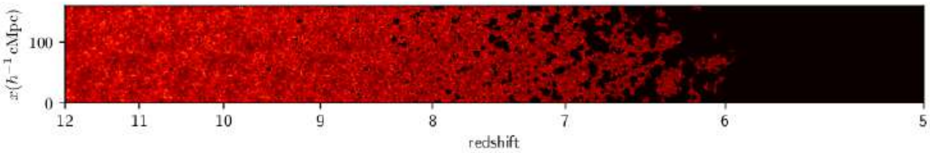

Figure 1.2: A lightcone map, obtained using a semi-numerical simulation of reionization. (Choudhury and Paranjape (2018))

other sources.

1.2 21cm Line

Hydrogen can trace the local properties of the gas because it is the most prevalent atomic species in the universe. The interaction of the magnetic moments of the proton and the electron results in the hyperfine splitting of the 1S ground state, which gives rise to the 21cm line of hydrogen. It has wavelength of 21.1 cm and a frequency of 1420 MHz, having two separate energy levels having a gap of $E = 5.9 \times 10^{-6} eV$ as a result of the splitting (Fig. 1.3). One of the few precisely measured quantity in astrophysics, this frequency was discovered through research on hydrogen masers (Goldenberg et al. (1960)). The so-called spin temperature, Ts, is determined by the relative populations of hydrogen atoms in the two spin states,

$$\frac{n_1}{n_0} = \frac{g_1}{g_0}\, exp\left\{\frac{-T_*}{T_s}\right\} \tag{1.1}$$

here n denotes the number density of atoms at the different levels, subscripts 1 and 0 denote the upper and lower atomic levels, g is the spin degeneracy factor of each state, $T_* \equiv E_{10}/k_B = 68mK$ is equivalent to the transition energy E_{10} .

The spin temperature T_s depends on the processes ongoing in the IGM. Hence to analytically calculate the spin temperature one needs to know all the physical processes taking place in IGM during the redshift of interest. In the regime of interest, $T_* << T_s$ hence all corresponding exponentials can be expanded to first order. For the 21-cm transition, $(g_1/g_0) = 3$, and since $T_* << T_s$, the excited state atoms have level population of 3 atoms out of 4 ($n_0 \approx n_1/3$).

1.3 Observing the 21cm line

Although the emission from Epoch of Reionization (EoR) is in centimeters, it gets redshifted to meter wavelengths because of the

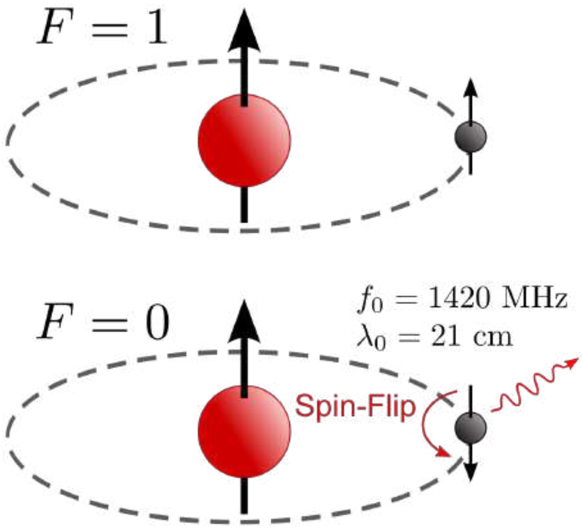

Figure 1.3: Ground state hyperfine levels of hydrogen. (Tiltec (2022))

expansion requiring radio frequency observations. The preferred design for 21 cm observations is an interferometer, which is made up of many dipole antennae as opposed to the single large dish that makes up a typical radio telescope. A beam can be created on the sky by cross-correlating the signals from various dipoles. Dipoles can be used to create arrays with very large collecting areas and a wide field of view, which are perfect for surveys. The intensity that we receive at the telescope does not correspond to the spin temperature but rather depends on the brightness temperature. Consider there is a hydrogen blob present somewhere along the line of sight. The universe is filled with cosmic microwave background, so when this radiation passes through the hydrogen cloud whose level population is decided by the spin temperature, the output intensity corresponds neither to CMB temperature T_γ nor to T_s, but correspond to the brightness temperature. The 21-cm brightness temperature can be written as,

$$T_b(\nu) = \frac{T_s - T_\gamma}{1+z}(1 - e^{-\tau_{\nu_0}})$$

$$\approx 27 x_{HI} (1+\delta) \left(\frac{H}{dv_r/dr + H}\right) \left(1 - \frac{T_\gamma}{T_s}\right) \left(\frac{1+z}{10 \; \dfrac{0.15}{\Omega_M} \; h^2}\right)^{1/2} \left(\frac{\Omega_b h^2}{0.023}\right) \tag{1.2}$$

where τ_{ν_0} is the optical depth at the 21-cm frequency ν_0 ; T_S is the gas spin temperature; H(z) is the Hubble parameter; δ(x, z) $\equiv \rho/\bar{\rho}$ - 1 is the evolved (Eulerian) density contrast; dv_r/dr is the comoving gradient of the LOS component of the comoving velocity; and all quantities are evaluated at redshift $z = \nu/\nu_0 - 1$. The final approximation makes the assumption that $dv_r/dr << H$, which is generally true for the redshifts and scale of interest.

Dipole-based observations have a high computational cost and, as a result of the long wavelengths, a poor angular resolution (Pritchard and Loeb (2012)). Due to the fact that the global 21cm signal is constant across numerous large patches of the sky, the telescopes do not require high angular resolution, even though there is a sizable amount of foreground to be taken into account.

1.4 Current status of Observations

Experimental 21cm observations have significantly increased over the past ten years (Liu and Shaw (2020)). Numerous techniques have been used to find spatial variations in cross-correlations with traditional galaxy surveys and to constrain the 21cm power spectrum (in case of post-reionization experiments). The following are a few of the telescopes that have been utilised in an effort to measure the 21cm signal: Some of the telescopes that have been used to try to measure the 21cm signal include the following:

- Giant Metrewave Radio Telescope (GMRT) : The first set of upper bounds at redshifts associated with reionization were presented by the GMRT Epoch of Reionization (GMRT-EoR) project. (Pen et al. (2009); Paciga et al. (2011);Paciga et al. (2013))

- Murchison Widefield Array (MWA) : The MWA has published a number of upper limits over a broad range of redshifts in recent years ranging from Cosmic Dawn redshifts to reionization redshifts (Dillon and Parsons (2016); Beardsley et al. (2016);Barry et al. (2019)).

- Precision Array for Probing the Epoch of Reionization (PAPER) : Operating between 100 and 200 MHz, PAPER has published a number of upper limits on the EoR power spectrum (Parsons et al. (2010);Jacobs et al. (2014))

- LOw Frequency Array (LOFAR) : Deep extragalactic surveys, transient phenomena, cosmic rays, solar science, cosmic magnetism, and cosmology are just a few of the important scientific projects that can be accommodated by the multi-purpose LOFAR observatory. Recently, it set upper bounds for both Cosmic Dawn (Gehlot et al. (2019)) and the EoR (Patil et al. (2017)).

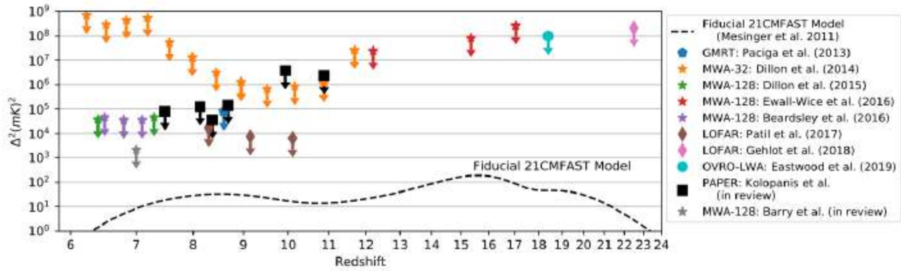

Figure 1.4: A summary of current upper limits on EoR power spectrum measurements. (Liu and Shaw (2020))

Although upper limits have tightened over time (Fig 1.4). there hasn't yet been a confirmed detection of the 21 cm autopower spectrum (i.e., not in cross-correlation with other probes). New telescopes with greater sensitivity are being developed, and the existing telescopes are being upgraded.

- The Hydrogen Epoch of Reionization Array (HERA) : When finished, it will have 350 dishes with a total diameter of 14 metres. It is intended to be sensitive enough to detect the 21 cm power spectrum with high significance both during reionization and after. (Liu and Parsons (2016)) and cosmic dawn (Kern et al. (2017)).

- The Square Kilometre Array (SKA). Of all the upcoming telescopes, the SKA represents the largest effort. SKA-low and SKA-mid, two separate telescopes, will make up the system (50–350 MHz). While there are still many unknowns surrounding the SKA, it is generally anticipated to have a robust scientific foundation, including the EoR (Koopmans et al. (2015)) and post-reionization cosmology (Zwart et al. (2015))

1.5 Need for Simulations

To interpret the data received from telescopes one needs to create a model that can be used to compare with the observations and then draw physical inference. Also, to make sure that the derived physical inferences are not biased one needs a model which is accurate as well efficient to explore and constrain the physically motivated parameter space. The models can be divided into three types, analytical models, full numerical simulations and semi-numerical approaches. The emergence of the first astrophysical objects and reionization could theoretically be modelled from the ground up, taking into account the intricate physical processes. A framework for comprehending the underlying physics that shapes the signal is provided by the analytical models used to calculate the 21cm signal. Additionally, they offer a technique for quickly investigating the dependence of the 21cm power spectrum on various astrophysical variables. In the end, interpreting observations necessitates a more thorough comparison of data to theoretical forecasts. While analytical studies highlight the general characteristics of the reionization process, the inhomogeneous, nonlinear, and non-gaussian processes call for intricate modelling and simulations of the ionisation and heated structure.

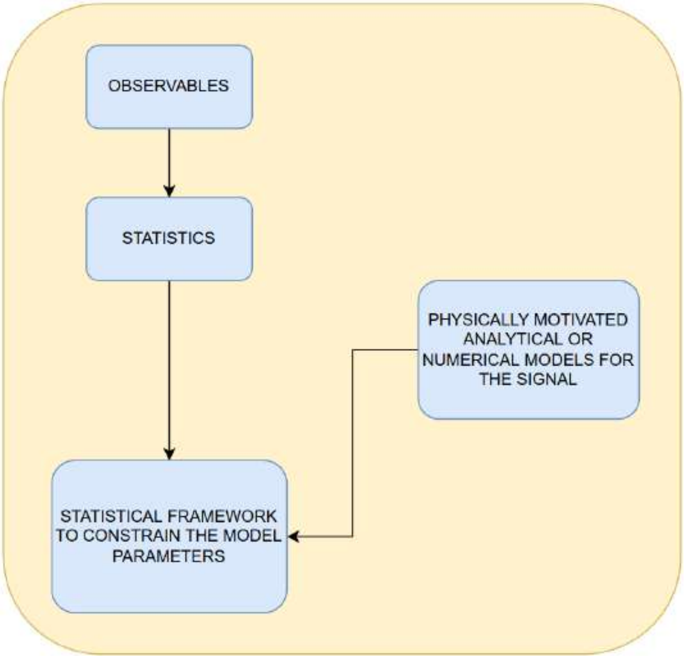

Figure 1.5: Block Diagram describing the process of interpreting the observation.

Numerous different techniques are available. N-body methods are needed to calculate the evolution of dark matter, hydrodynamical methods are needed to model the gaseous component, and a radiative transfer algorithm is needed to calculate the evolution of the ionised structure. Although accurate, these simulations require a lot of computational resources. Semi-numerical approaches are taken into consideration in order to get around the drawbacks of both analytical and fully numerical approaches. These models lie somewhere between the two models, and try to bring out the best features of both the models. The current generation semi-numeric simulations, however, lack the required accuracy that the SKA will demand in the near future thanks to its high sensitivity and resolution. Moreover, the simulations take certain approximations to increase the computational efficiency which may not be entirely correct and can have significant consequences on the derived statistics. Hence, there is a need for an accurate model which has fewer approximations and at the same time is not computationally heavy. This thesis focuses on improving this particular aspect of the semi-numerical simulations for cosmic dawn 21-cm signal by incorporating accurate treatment of the IGM physics.

Chapter 2

21cm Physics

The spin temperature is crucial for the 21 cm signal's ability to be detected. A signal can only be seen if this temperature differs from the ambient temperature. The spin temperature is determined by three processes,

- Absorption/emission of 21cm photons from and to the radio background.
- Collisions with other atoms and with electrons.
- Scattering of Ly-α photons can cause a spin-flip transition.

Assuming that timescales of interest are all much shorter than the expansion time, the spin temperature can be found using equilibrium approximation,

$$T_s^{-1} = \frac{T_\gamma^{-1} + x_c T_k^{-1} + x_\alpha^{-1} T_c^{-1}}{1 + x_c + x_\alpha} \tag{2.1}$$

where T_γ is the temperature of the surrounding radio photons, generally equal to the CMB temperature, which depends only on redshift. The kinetic temperature T_k depends on the processes that take place in the IGM during the redshift of interest. The third factor, color temperature T_c, comes into play via the wouthuysen-field effect and depends on the effective temperature of the UV radiation field. Here x_c and x_α are the collisional and Lyman-α coupling coefficients which signifies how much these temperatures affect the spin temperature.

2.1 Background Radiation

For the 21cm spin temperature modelling, two categories of background radio sources are crucial. Firstly, one can use the CMB as a radio background source. The 21cm feature is interpreted in this instance as a spectral distortion of the CMB blackbody. The CMB is essentially a uniform source because temperature variations are of the order of 10^{-5}. In order to create a 3D map, observations at various frequencies probe various spherical shells of the observable universe. Additionally, since the CMB temperature only depends on the redshift, it is simple to model.

The radio-loud point sources, such as a radio-loud quasar, are the second type. The gas will be visible in absorption against the sources in this scenario because the source will be much brighter than the 21cm signal. The "21cm forest," so named in analogy to the Lyα forest, results from the presence of lines from neutral regions at various distances along the LoS. The high background brightness makes it possible to use the 21cm forest to study the IGM's high frequency resolution probing small-scale structure.

2.2 Collisional Coupling

Collision of hydrogen atoms with different particles have the means to induce spin-flips in the hydrogen atom thereby making the collisional coupling significant in the early Universe where the gas density is high. The coupling coefficient for collisions with species i is given by

$$x_c^i \equiv \frac{C_{10}^i}{A_{10}} \frac{T_*}{T_\gamma} = \frac{n_i \kappa_{10}^i}{A_{10}} \frac{T_*}{T_\gamma} \tag{2.2}$$

where C_{10} is de-excitation rate for collisions, A_{10} is the einstein A coefficient for de-excitation, n_i is the species number density, T_* is the excitation temperature and κ_{10}^i is the rate coefficient for spin de-excitation in collisions with that species. The total x_c is the sum over all species i, which in principle includes collisions with (1) other hydrogen atoms, (2) free electrons, (3) protons, and (4) other species (helium and deuterium); the last turn out to be unimportant. These rate coefficients are determined by the quantum mechanical cross sections of the relevant processes. The results can be seen in Figure 2.1, note that the net rates are also proportional to the densities of the individual species, so H-H collisions still dominate in a weakly-ionized medium. Despite having a small atomic cross-section, neutral hydrogen atom collisions predominate in the unperturbed IGM when the ionised fraction is low. In partially ionised gas, free electrons are significant; collisions with protons only matter at the lowest temperatures. The formula for the total collisional coupling coefficient is,

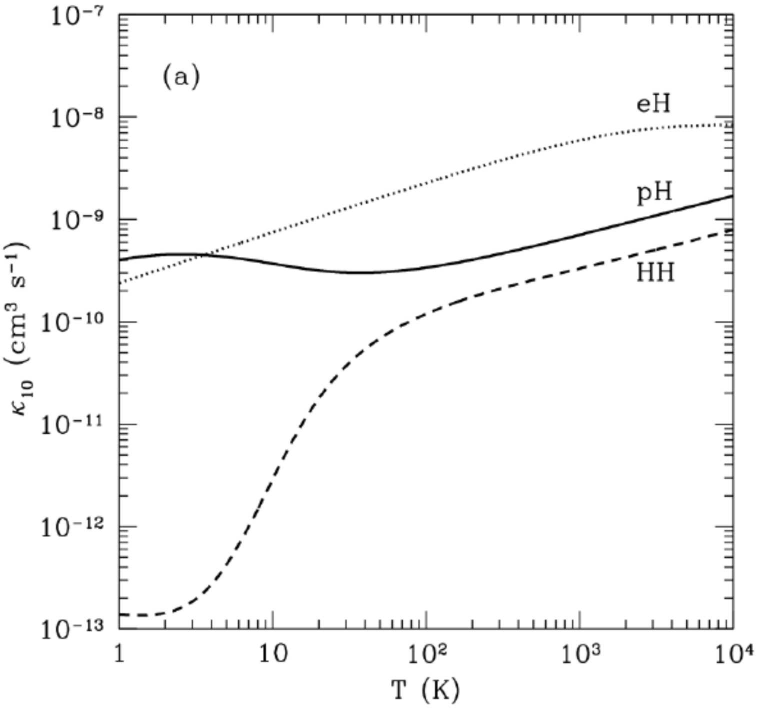

Figure 2.1: De-excitation rate coefficients (Image credit: Furlanetto (2007)).

$$x_c = x_c^{HH} + x_c^{eH} + x_c^{pH} = \frac{T_*}{A_{10}T_\gamma}\left[\,\kappa_{1-0}^{HH}(T_k)n_H + \kappa_{1-0}^{eH}(T_k)n_e + \kappa_{1-0}^{pH}(T_k)n_p\,\right] \tag{2.3}$$

where κ is the scattering rate between hydrogen atom and other species. The collisional rates require a quantum mechanical calculation. Collional coupling dominate during the cosmic Dark ages as the universe was dense enough for collisions to happen frequently.

2.3 The Wouthuysen-Field Effect

Collisional coupling of the 21cm line is ineffective for the majority of redshifts that will be observationally probed. Resonant scattering of the Ly$alpha$ photons, on the other hand, offers another pathway for coupling once star formation starts. This process is known as the Wouthuysen-Field (WF) effect (Wouthuysen (1952))

Consider the case where a Lyman α photon is absorbed by a hydrogen atom that is in the hyperfine singlet state (see Fig. 1.3 for reference). F = 0, 1 is permitted by the electric dipole selection rules, but F = 0 to 0 is not (here F is the total angular momentum of the atom). From this point, the atom can be de-excited to one of the two ground state hyperfine levels by the emission of a Lyα photon. But under the same conditions, this state can degenerate to the $_1S_{1/2}$ triplet level. As a result, atoms are capable of switching between hyperfine states by spontaneously absorbing and reemitting Lyman-α photons. The fraction $f_{rec}(n)$ of cascades that end in Lyman-α photons is the crucial quantity for figuring out the coupling induced by these photons. Higher Lyman-n levels can exhibit the same phenomenon. The WF effect's physics are much more intricate than this straightforward explanation would imply. The coupling may be written as,

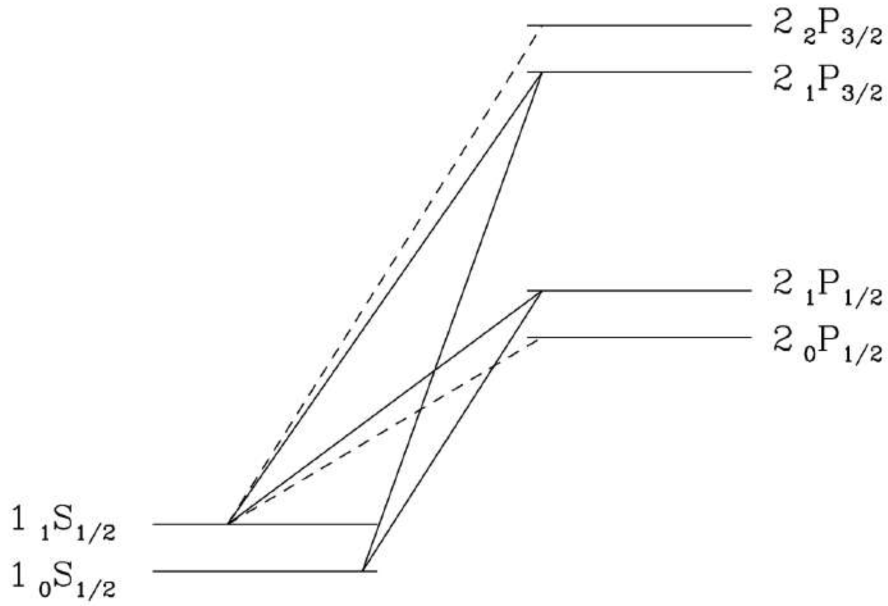

Figure 2.2: Level diagram illustrating Wouthuysen-Field effect. (Image credit: Pritchard and Furlanetto (2006)).

$$x_\alpha = \frac{4P_\alpha}{27A_{10}}\frac{T_*}{T_\gamma} \tag{2.4}$$

where P_α is the scattering rate of Lyα photons. The rate at which Lyα photons scatter from a hydrogen atom is given by,

$$P_\alpha = 4\pi\chi_\alpha \int d\nu J_\nu(\nu)\phi_\alpha(\nu) \tag{2.5}$$

where $\chi_\alpha \equiv (\pi e^2/m_e c)f$ is the oscillation strength of the Lyα transition, $\sigma_\nu \equiv \chi_\alpha\phi_\alpha(\nu)$ is the local absorption crossection, $J_\nu(\nu)$ is the angle-averaged specific intensity of the background radiation field and $\phi_\alpha(\nu)$ is the Lyα absorption profile . Using this expression, one can express the coupling as,

$$x_\alpha = \frac{16\pi^2 T_* e^2 f_\alpha}{27A_{10}T_\gamma m_e c} S_\alpha J_\alpha \tag{2.6}$$

where J is the specific flux evaluated at the Lyα frequency and $S_\alpha \equiv \int dx \phi_\alpha(x) J_\nu(x)/J_\infty$ with J_∞ being the flux away from the absorption feature, as a correction factor of order unity that describes the detailed structure of the photon distribution in the neighborhood of the $Ly\alpha$ resonance.

The physics described above relates the spin temperature to the radiation field's colour temperature, which is a measurement of the radiation field's shape as a function of frequency in the vicinity of the $Ly\alpha$ line defined by (Rybicki (2006))

$$\frac{h}{k_b T_c} = -\frac{dlogn_\nu}{d\nu} \tag{2.7}$$

where $n_\nu = c^2 j_\nu / 2\nu^2$ is the photon occupation number. The optical depth to $Ly\alpha$ scattering is typically very large, leading to a large number of scatterings, which causes the radiation field and the gas to enter local equilibrium (Field (1959)). Although photons scatter as they enter the $Ly - \alpha$ resonance, one would anticipate that the net flow rate would remain unchanged because the cross-section is symmetric. However, because the recoil of the atom causes $Ly - \alpha$ photons to lose some of their energy, an asymmetry is created that forces the distribution into local thermal equilibrium with $T_c \approx T_k$.

The above discussion has looked over the processes whereby the distribution of photons is changed by the spin-flip transitions. This greatly increases the difficulty of determining T_s and T_c because it requires them to be iterated in order to find a level-population solution that is self-consistent.

2.4 Outline of Global 21cm signal

The cosmological context of the 21cm signal will be the main topic of this section. A model for the global evolution and fluctuations of the four variables that make up the 21cm brightness temperature, $T_b(T_k,\ x_i,\ j_alpha,\ n_H)$, is necessary to calculate the 21cm signal. One of the key characteristics of T_b is that its dependence on these variables can be dissociated since each of these quantities reaches a point of saturation. For example, once the $Ly\alpha$ flux is high enough, the spin and kinetic temperatures saturate and any further variation in the J_α becomes irrelevant to the signal's specifics. These various regimes are depicted in a schematic form is shown in Fig.2.3. There may be overlap between these epochs because the majority of them are not clearly separable.

- $200 \leqslant z \leqslant 1100$: Compton scattering maintains thermal coupling of gas to the CMB, setting $T_k = T_y$. High gas density leads to effective collisional coupling so $T_s = T_\gamma$ and hence $T_b = 0$.

- $40 \leqslant z \leqslant 200$: Gas cools adiabatically leading to $T_k < T_y$, collisional coupling sets $T_s < T_\gamma$ leading to $T_b < 0$ i.e absorption signal.

- $z_* \leqslant z \leqslant 40$: Expansion continues, decreasing the gas density, collisional coupling becomes ineffective and radiative coupling sets $T_s = T_\gamma$. No detectable signal.

- $z_\alpha \leqslant z \leqslant z_*$: First sources start emitting both $Ly\alpha$ and x-rays at z_*. Emissivity required for $Ly\alpha$ coupling is significantly less than that for heating T_k above T_γ. $T_s \approx T_k < T_\gamma$ and there is an absorption signal.

- $z_h \leqslant z \leqslant z_\alpha$: $Ly\alpha$ coupling saturates, heating becomes significant, T_k starts increasing but remains below T_γ and the gas temperature fluctuation dictates T_b fluctuations. Absorption signal is observed till $T_k = T_\gamma$ at z_h.

- $z_T \leqslant z \leqslant z_h$: After the heating transition, $T_k > T_\gamma$, emission signal is seen. At z_T , $T_s \approx T_k >> T_\gamma$.

- $z_r \leqslant z \leqslant z_T$: Heating make $T_k >> T_\gamma$ and temperature fluctuations become unimportant. $T_s \approx T_k >> T_\gamma$ and the dependence of T_s may be neglected in equation . Ionization fluctuations dominate the 21cm signal

- $z \leqslant z_r$: After reionizations, any leftover 21cm signal originates primarily from damped $Ly\alpha$ systems.

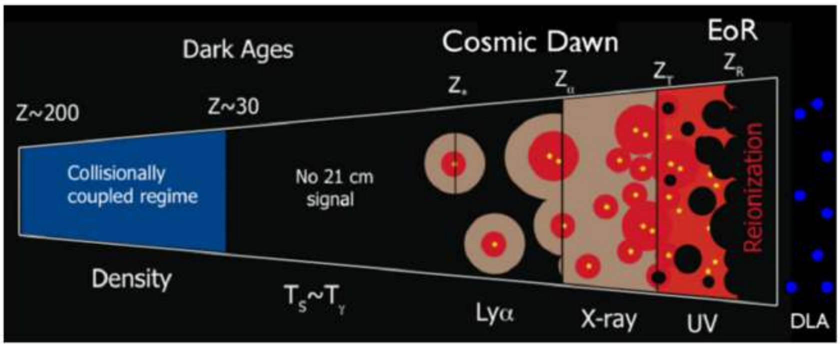

Figure 2.3: Cartoon of the different phases of the 21 cm signal.(Image credit: Pritchard and Loeb (2012)).

2.5 Evolution of global signal

The previous section focused on the qualitative evolution of the signal, this section will describe the details of making quantitative prediction. The IGM will be treated as a two phase medium to simplify the calculations. The initial phase of the IGM is a single, largely neutral phase that was left over from recombination. Two factors, gas temperature T_k and a small percentage of free electrons (x_e), define this phase. This phase is responsible for producing the 21cm signal.

Following the formation of galaxies and stars, the UV photons begin ionising the nearby HII regions. The ionised regions have a very sharp boundary because UV photons have a short mean free path. As a result, provided that the free electron fraction is low, the ionised bubbles can be thought of as a second phase in the IGM with a volume filling factor x_i that is roughly equal to the mean ionisation factor. The bubbles in this case are thought to be fully ionised. One can treat the $Ly\alpha$ flux J_α as being the same in both phases because the photons that redshift into the $Ly\alpha$ resonance initially have a long mean free path. As a result, four values x_i, x_e, T_k and J_α are to be calculated. The evolution equation for $T_k(x,z)$ and the local ionized fraction in the neutral phase IGM, $x_e(x,z)$ can be written as ,

$$\frac{dx_e(\mathbf{x},z)}{dz} = \frac{dt}{dz}\left[\Lambda_{ion} - \alpha_A C x_e^2 n_b f_H\right] \tag{2.8}$$

$$\frac{dT_k(\mathbf{x},z)}{dz} = \frac{2}{3k_b(1+x_e)}\frac{dt}{dz}\sum_p \epsilon_p + \frac{2T_k}{3n_b}\frac{dn_b}{dz} - \frac{T_k}{1+x_e}\frac{dx_e}{dz} \tag{2.9}$$

where n_b is the total (H + He) baryonic number density at ($\mathbf{x}$,z), $\epsilon_p(x,z)$ is the heating rate per baryon for process p in erg s^-1, Λ_{ion} is the ionization rate per baryon, α_A is the case-A recombination coefficient, $C \equiv < n^2 > / < n >^2$ is the clumping factor, k_b is the boltzmann constant, f_H is the hydrogen number fraction. In equation 2.9, the first term corresponds to the heat input, the second term accounts for adiabatic cooling of the gas due to cosmic expansion and the last term corresponds to the change in the total number of gas particles due to ionizations. It is important to point that the two phase approximation breaks down when the value of x_e becomes close to unity indicating that most of the IGM has been ionized and there is no clear distinction between the ionized bubble and a neutral bulk IGM.

2.6 Heating and Ionization

The heating rate can be determined by integrating 2.9 but one needs to know which heating mechanisms are relevant for the redshift of interest. Compton heating of the gas predominates at high redshifts. This results from the small residual free electron fractions scattering the CMB photons. Compton heating couples T_k to T_γ for $z \geq 150$, but loses its effectiveness below this redshift. Thus it sets the initial conditions before stars start forming. The heating rate per baryon for Compton heating is given by Naoz and Barkana (2005),

$$\frac{2}{3}\frac{\epsilon_{Compton}}{k_B n} = \frac{x_e}{1 + f_{He} + x_e}\frac{T_\gamma - T_k}{t_\gamma}\frac{u_\gamma}{\bar{u_\gamma}}(1+z)^4 \tag{2.10}$$

where $f_H e$ is the helium fraction, u_γ is the energy density of the CMB, $\sigma_T = 6.65 \times 10^{-25}\ cm^2$ is the Thomson cross-section, and t_γ is defined as,

$$t_\gamma^{-1} = \frac{8\bar{u_\gamma}\sigma_T}{3m_e c} = 8.55 \times 10^{-13}\ yr^{-1} \tag{2.11}$$

There are numerous sources of heat available at lower redshifts. One possibility is the shocks brought on when gas separates from the Hubble flow and is associated with large-scale structure. Such shocks can be significantly important at late times Furlanetto and Loeb (2004). Another heating source can be the scattering of the $Ly\alpha$ photons off hydrogen atoms, leading to a slight recoil of the nucleus that takes energy from the photons. This can be a significant heating option, but it necessitates extremely high Ly-alpha fluxes, making it most pertinent in more recent times (Madau et al. (1997)). The most important source of energy injection into the IGM is via x-ray heating of the gas Chen and Miralda-Escude (2004). Once compact objects are formed, x-ray photons can be produced in large quantities because they have a long mean free path and can heat the gas far from the source. By photoionizing H I and He I, X-rays heat the gas primarily. This produces energetic photoelectrons, which release their energy through heating, secondary ionizations, and atomic excitation.It is possible to express the overall rate of energy deposition per baryon as,

$$\epsilon_x = 4\pi \int d\nu J_\nu \sum_i (h\nu - E_i^{th}) f_{heat} f_i x_i \sigma_{\nu,i} \tag{2.12}$$

where summation is over the species i = H I, He I and He II, n$_i$ is the number density of species i, x_i is the cell's species neutral fraction, E_i^{th} is the ionization threshold energy of species i, σ_ν, i is the cross-section for photoionization. The factor f_{heat} is defined as the fraction of energy enegry deposited as heat and J$_\nu$ is the number flux of photons of frequency ν

Chapter 3

Simulations

Now that the underlying physics has been described, the next step is to incorporate these equations into the simulation. In principle it is possible to model all these equations in a numerical fashion and evolve the equation over the redshift duration. In practice however, simulating these epochs requires enormous simulation boxes. In order to statistically model ionised regions, gigaparsec scales are required. However, the resolution needs to be accurate enough to distinguish between the underlying sources and sinks of ionising photons as well as the intricate small-scale feedback mechanisms that control them. Once you have a simulation that is self-consistent, it can be then used as a tool to interpret the data from the telescopes. As mentioned in section 1.5 there are several techniques to achieve this. This chapter will briefly explain all these techniques and go into the details of the state-of-the-art simulations publicly available.

3.1 Radiative Transfer Simulations

Radiative transfer (RT) codes are programs that numerically simulate the propagation of electromagnetic radiation through a medium. For tracking the ionization state, it works by tracing rays from all sources and iteratively solving the equation 2.8 by converting it into numerical equation. Since they account for the ionisation and recombination processes along each individual photon's path, Radiative transfer codes are able to produce an accurate reionization topology and history. Radiative transfer is the most computationally expensive part of a reionization simulation due to the problem's high dimensionality. The algorithm must scale nearly linearly with the resolution of the simulation, as is the case with N-body and hydrodynamics algorithms, in order to implement a radiative transfer scheme with a mass and spatial resolution as high as those featured in contemporary galaxy formation runs.

A 3D radiative transfer method which has been widely used is 'Conservative Causal Ray-tracing method' (C^2-ray) (Iliev and Mellema (2006)). The algorithm is as follows, it first prepares a source list in a random order at each redshift. Then taking into account the SED of sources, the total photo-ionization rate (Γ) is calculated at each cell at time t. To calculate this term, the neutral fraction of each cell is required, which calculated by evolving the following equation,

$$\frac{dx_{HII}}{dt} = (1 - x_{HII})(\Gamma + n_e C_H) - x n_e C \alpha_H \tag{3.1}$$

where n_e is the electron density at the cell, C_H and α_H are the collisional ionization and recombination coefficients for hydrogen respectively. The quantity C is the clumping factor which accounts for the clumpiness of the IGM. Other than C^2-ray, other fully radiative transfer codes are also present (Iliev et al. (2008) and Harnois-Deraps et al. (2013))

To mitigate the time inefficiency, a simplified approach was developed by Thomas and Zaroubi (2008) and later evolved into the GRIZZLY code (Ghara et al. (2018)). In this algorithm, only one ray is used for each search, instead of utilizing the full ray-tracking, with the density profile along the ray being the spherical average over all the directions. The radiative transfer code is then solved along that ray in "1D", as a consequence all the ionized regions around the sources are spherical. Ghara et al. (2018) has shown that this approach is a useful approximation for modeling the 21cm emission during reionization. However, such an approach fails to capture the "outside in" stage of reionization (Gnedin and Madau (2022)). For comparison between 3D and 1D radiative transfer codes refer Ghara et al. (2018).

3.2 Semi-numerical Simulations

Analytical models, on the other hand, are quick and provide information about various processes. These models, however, are unreliable outside of the linear regime due to the approximations taken into account. Additionally, analytical models only offer straightforward predictions like the power spectrum, probability density function, and mean 21-cm signal. Therefore, you need a model that combines the best features of both, which is where semi-numerical simulations come into play.

Consider two models - the crudest and the finest model. The crudest model is the analytical model, for example the global 21-cm brightness temperature graph (2.3). Whereas the finest model would be a completely numerical model that satisfies a variety of statistics for a large number of test cases. The semi-numeric approach lies somewhere between these two. It has to satisfy the results of the crudest model. This is a necessary condition but not sufficient to call it semi-numeric. It should also satisfy at least some basic statistical results of the finest model and then one can calibrate the semi-numerical model, so that it can be safely used for other statistics as well. ()

For these simulations, precise knowledge of the entire nonlinear matter distribution from numerical simulations is not necessary. The Gaussian random field of the initial conditions or their direct derivative, such as the second order perturbation theory, provide direct information about the spatial distribution of H II regions. The majority of semi-numerical techniques for simulating EoR compare the average number of photons in a given volume with the average number of neutral hydrogen present in that volume. The semi-numeric code has no interest in individual photons. Because realisations are computationally less expensive than radiative transfer codes, semi-numerical models can be effectively used to constrain the broad parameter space.

3.3 Which approach to choose?

Lot of work has already been done to understand the physical processes to be simulated. There are several ab initio simulations as well as semi-numerical simulations available in industry. Both of them have their pros and cons and depending on the requirements one method can be preferable over the other. The ionisation and recombination processes that occur along each individual photon's path are taken into account by the radiative transfer codes, which allows them to produce accurate realisations of cosmic dawn and EoR. However, they need a tremendous amount of computational time to complete this feat (hundreds of thousands of core hours). Since the parameter space for the reionization models is largely unknown, it is not practical to use this approach in that situation. Additionally, the majority of the current and upcoming radio interferometric surveys, including the SKA, won't be sensitive enough to deliver data with a resolution on par with the ab initio simulations.

On the contrary, the semi-numeric approach can simulate a reasonable volume of the universe (comparable to the survey volume of LOFAR or SKA) in a few minutes of computational time on a single processor with considerably less memory consumption (few gigabytes of RAM). At relevant scales, k $< 0.50\ Mpc^{-1}$, the redshifted 21-cm signal as calculated using semi-numerical simulations match pretty well with those of the radiative transfer codes (Majumdar et al. (2014)). Hence we will move forward with the semi-numerical approach to calculate the spin temperature fluctuations and, eventually, create brightness temperature maps of the HI-21 cm signal. The rest of the chapter will discuss various publicly available semi-numerical simulations for 21cm signal from Cosmic dawn and EoR.

3.4 21cmFAST

The most widely used semi-numerical model is perhaps the 21cmFAST code (Mesinger et al. (2010)). It uses the excursion set-based formalism of Furlanetto et al. (2004) to create a realization of the distribution of ionized gas at any given redshift. The density field is obtained using the Zel'dovich approximation. This makes the whole process a lot faster as there is no N-body particle evolution involved. This approach of generating the density fields has been adopted by Choudhury et al. (2009) and it was shown that the resulting field at high z traced the DM distribution from an N-Body fairly well. To increase the speed and dynamic range, 21cmFAST uses FFRT algorithm, which uses the conditional Press-Schechter (PS) formalism directly on the density field, thereby avoiding the need to resolve halos. One needs the velocity field to take care of the redshift space distortion while calculating the differential brightness temperature (eq. 1.2). Since there is no particle field, a pseudo velocity field is calculated using the Zel'Dovich approximation on the 3D realizations. In this first-order perturbation theory, the velocity field can be written in k-space as,

$$\mathbf{v}(\mathbf{k}, z) = \frac{i\mathbf{k}}{\mathbf{k^2}}\dot{D}(z)\delta(k) \tag{3.2}$$

where $\dot{D}(z)$ is the time derivative of the growth factor and $\delta(k)$ is the fluctuation in density field. 21cmFAST takes into account the underlying astrophysical process by modeling the equations that were described in chapter 2 in a numerical fashion. It also includes a special correction to overcome photon conservation issue (Park et al. (2022)). 21cmFAST is hence able to simulate the pre-reionization regime and is used ,for example, by the Murchison Widefield Array (MWA), LOw-Frequency ARray (LOFAR) and Hydrogen Epoch of Reionization Array (HERA), to model the large-scale cosmological 21-cm signal. In particular, the speed of 21cmFAST is important to produce simulations that are large enough (several Gpc across) to represent modern low-frequency observations.

3.5 ReionYuga

ReionYuga is an open-source code to generate the Epoch of Reionization (EoR) neutral Hydrogen (HI) field (successively the redshifted 21-cm signal) within a cosmological simulation box (Mondal et al. (2021)). This is a semi-numerical simulation that couples with the N-Body and FoF Halo finder codes. One of the benefits of ReionYuga is that it implements the algorithm on the density field generated using the N-body and then identifies the Halo using the FoF algorithm, making the outputs more accurate. The code is based on excursion set formalism and uses a three parameter model. The code is based on excursion set formalism and uses a three parameter model. This method assumes that the total number of ionizing photons contributed by a halo of mass M_h is,

$$N_\gamma(M_h) = N_{ion} M_h \tag{3.3}$$

where N_{ion}, is a dimensionless constant which effectively represents the number of photons entering in the IGM per baryon in collapsed objects. Once the locations and masses of the halos are known as a functional form for , the ionizing photon field can be constructed. A cell is flagged to be ionized if it satisfies following equation,

$$< n_\gamma(x) >_R \ \geq \ < n_H(x) >_R \tag{3.4}$$

where R is the smoothing radius, is the average number density of photons and is that for hydrogen. It also keeps track of partial ionization, by setting the ionization fraction to $< n_\gamma(x) > / < n_H(x) >$. Since the mean free path of UV photons is not large, around 20 cMpc, and because the density field does not vary much over a light travel time corresponding to this scale, the ionization field for a particular redshift will depend on the density field on only that redshift. So, the field is smoothed from the cell size to that corresponding to the mean free path, and the corresponding ionization field is calculated. An important point to note is that ReionYuga presumes as a preheated IGM, thereby avoiding the need to implement astrophysical processes like X-ray heating and Lyα coupling. This is a good enough assumption for the EoR period but if one needs to probe the cosmic dawn era these processes become relevant.

3.6 SCRIPT

In any model of reionization, the number of hydrogen atoms ionized must be equal to the number of ionizing photons produced by the sources (compensated for recombination). Alvarez (2016) and Paranjape et al. (2016) have shown that the Excursion-Set (ES) models violate this equality because the number of ionizing photons are not conserved. The ES models' exclusive focus on average quantities rather than the stochastically fluctuating source counts is the root cause of this lack of conservation. In order to understand the consequences of photon non-conservation one needs to plot the measure of photon non-conservation, $\zeta f_{coll}/Q^M_{HII}$ against Q^M_{HII}. This causes some level of bias non-convergence as a function of map resolution in the ES method.

To mitigate this problem, Paranjape et al. (2016) came up with "Semi-numerical Code for ReionIzation with PhoTon Conservation"

(SCRIPT). The photon conservation is achieved in SCRIPT by explicitly obeying the following equality throughout the simulation.

$$Q^M_{HII} = \zeta f_{coll}(x) \tag{3.5}$$

where Q^M_{HII} is the mass-averaged ionization fraction, ζ is the effective ionization efficiency and $f_{coll}(x)$ is the collapse fraction. Following is the simple description of the algorithm used in SCRIPT,

- Assign ionizing fraction according to the ionization criterion in each cell allowing for over-ionization.
- Redistribute the photons from over-ionized cells to the neighbouring cells which are yet to be ionized.

SCRIPT has been further evolved to constrain the reionization and thermal history of the Universe (Maity and Choudhury (2022))

Chapter 4

Implementing X-Ray Heating

After a comprehensive explanation of all the relevant physical processes and the simulation techniques, it is now time to implement all these into a self-consistent simulation and then analyze the results. The formalism to implement these processes is motivated by the 21cmFAST and the ReionYuga simulations. The goal here is to develop a semi-numerical simulation which can be used to constrain the Cosmic Dawn and EoR parameters by performing fourier domain (power spectrum, bispectrum) or real space (Largest cluster statistics, Minkowski functions) statistical analysis.

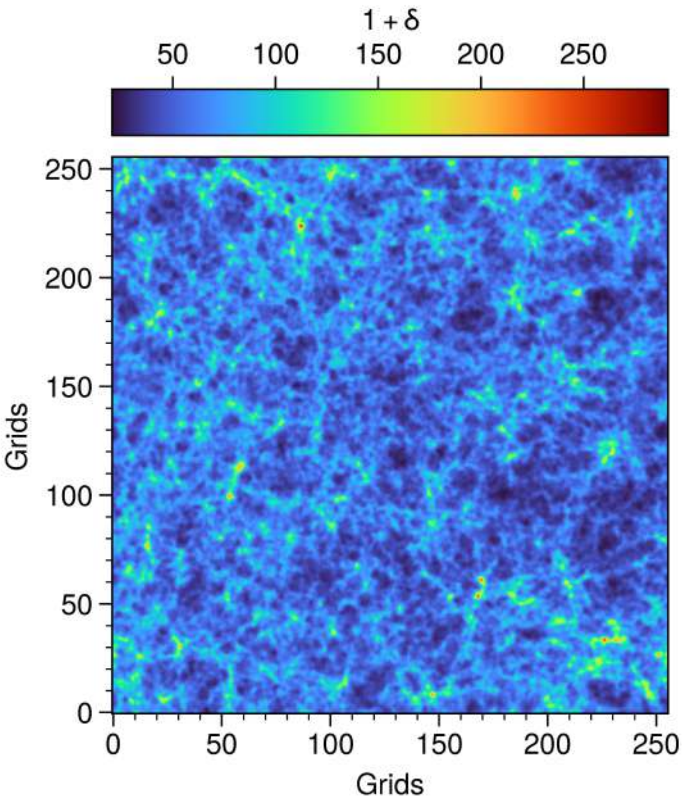

Figure 4.1: Dark Matter density field smoothed to a 256^3 grid.

4.1 Ingredient Fields

The dark matter density field is calculated using the N-Body simulation prescribed by Bharadwaj and Srikant (2004), which is based on Particle mesh scheme. The simulation considered here has a simulation volume of $(143.36\ cMpc)^3$ with a fine grid resolution of 2048^3 cells. The number of N-body particles was 1024^3 having mass of around $1.089 \times 10^8\ M_\odot$. For each output from the N-body simulations, halos were identified using the Friends-of-Friend algorithm as prescribed by Mondal et al. (2015). The minimum halo mass identified corresponds to 10 particles with a total mass of $10^9\ M_\odot$. After constructing the Halo list, the output fields are then smoothed onto a grid with 256^3 cells onto which further formalism is imposed. The standard Λ-CDM model is considered with $(\Omega_\Lambda,\ \Omega_M,\ \Omega_b, n, \sigma_8, h)$ = (0.6704, 0.3183, 0.04902, 0.9619, 0.8347). The figures Fig.4.1 and 4.2 below show the smoothed fields.

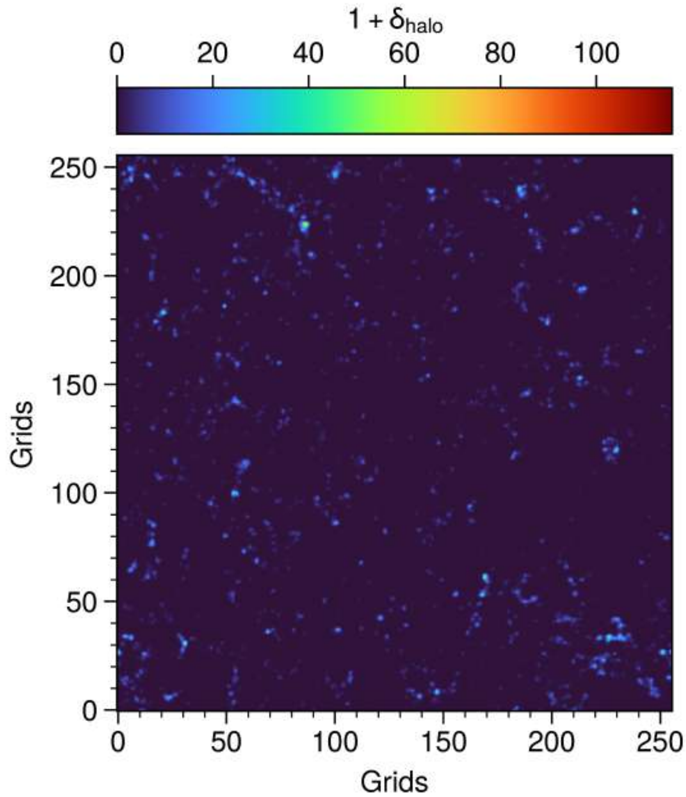

Figure 4.2: Halo Map smoothed to a 256^3 grid.

4.2 Photon flux

To calculate the heating rate per baryon one needs the number flux of photons (see eq. 2.12). This section will describe in detail how this field is calculated in the simulation. The X-ray number flux can be written as the following (Pritchard and Furlanetto (2007)),

$$J_X(z) = \int_z^\infty dz' \frac{(1+z)^2}{4\pi} \frac{c}{H(z')} \hat{\epsilon_x}(\nu', z') \, e^{-\tau} \tag{4.1}$$

where $\hat{\epsilon_x}(\nu, z)$ is the comoving photon emissivity for the X-ray sources, H(z) is the Hubble function and ν' is the emission frequency at z' corresponding to an X-ray frequency ν at z,

$$\nu' = \nu \frac{(1+z')}{(1+z)} \tag{4.2}$$

The optical depth is given by,

$$\tau(\nu, z, z') = \int_z^{z'} \frac{dl}{dz''} dz'' [n_{HI}\sigma_\nu + n_{HeI}\sigma_\nu + n_{HeII}\sigma_\nu] \tag{4.3}$$

The emissivity is proportional to the Star Formation Rate Density (SFRD) and is given by,

$$\hat{\epsilon_x}(\nu, z) = \hat{\epsilon_x}(\nu) \left(\frac{SFRD}{M_\odot yr^{-1} Mpc^{-3}} \right) \tag{4.4}$$

where,

$$\hat{\epsilon_x}(\nu) = \frac{L_0}{h v_0} \left(\frac{\nu}{\nu_0} \right)^{-\alpha-1} \tag{4.5}$$

where ν_0 is lowest X-ray frequency escaping into the IGM, α is the power law index of the spectral distribution function. The value of L_0 is set to 3.4×10^{40} f_X $ergs^{-1}Mpc^{-3}$ (Pritchard and Furlanetto (2007)), where f_X is a highly uncertain constant factor. This normalization is chosen so that at $f_X = 1$, the total X-ray luminosity per unit SFR is consistent with that observed in star-burst galaxies in the present epoch (refer Furlanetto (2007) for more details). So, to find the photons flux one needs to know the SFRD. In this simulation Star Formation Density (SFD) will be calculated instead of SFRD, the dt derivative will be absorbed in the kinetic temperature evolution (eq. 2.9). SFD is proportional to the change in collapse fraction, which can be represent using the halo mass catalog, with respect to the redshift,

$$SFD = N_X \frac{dM_h}{dz} \tag{4.6}$$

where N_X is the proportionality constant, a parameter which can be tuned in the simulation and M_h is the mass of the halo. So the final equation to calculate the photon number flux is,

$$J_X(z) = \frac{(1+z)^2}{4\pi} \frac{L_0 c}{h\nu_0} N_X \left(\frac{\nu}{\nu_0} \right)^{-\alpha-1} \int_z^\infty dz' \left(\frac{dM_h}{dz'} \right) \frac{1}{H(z')} \tag{4.7}$$

For simplicity, the attenuation due to IGM is ignored and will be incorporated later.

4.3 Heating Fraction

As mentioned in sec 2.6, the interaction of the energetic electrons with the atoms lead to three effects namely excitations, secondary ionizations and heating. One needs to know how much fraction of energy is lost via heating to calculate the heating per baryon (eq. 2.12), i.e the value of f_{heat}. There is no straightforward way to calculate this fraction using physics, Furlanetto and Stoever (2010) provides a complete treatment of this process using a MCMC model. As lower energy particles can only interact with the electron gas and will therefore deposit all of their energy as heat, the model starts with a single electron with energy $E > 10.2eV$. They follow 10^5 input electrons at 258 logarithmically spaced energies between 10 and 9900 eV, at each of 14 ionised fractions between 10^{-4} and 0.999, to obtain their final result. The results of the model for the heating fraction are displayed in the plots below.

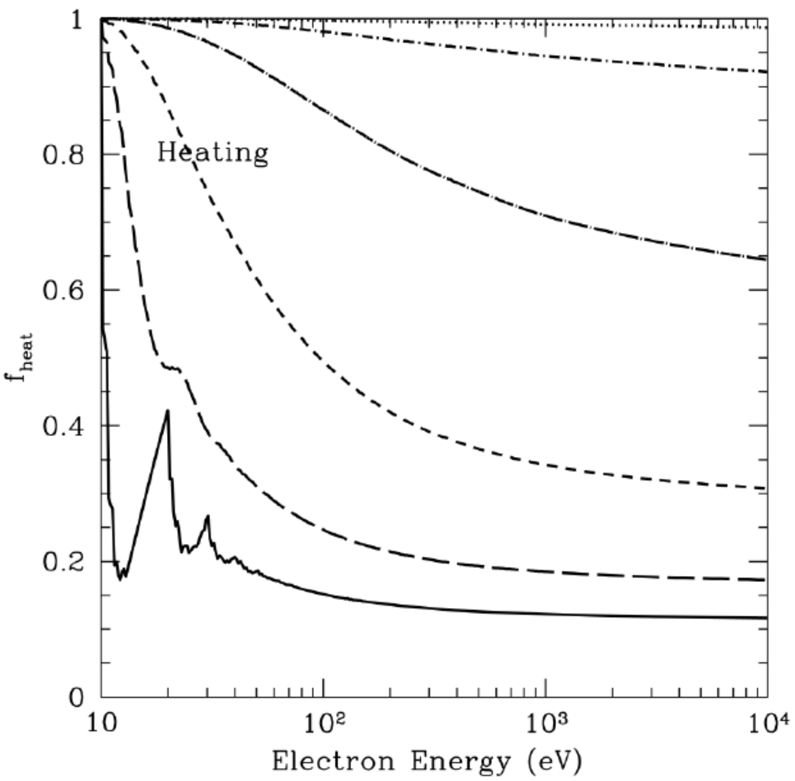

Figure 4.3: Heating fraction at $x_i = 10^{-4}$, 10^{-3}, 10^{-2}, 10^{-1}, 0.5, 0.9 from bottom to top. (Image credit : Furlanetto and Stoever (2010))

In fig. 4.3 the energy injected as heat decreases and the energy of ionisation increases as E rises because more and more excitation and ionisation processes are made possible. At higher energies, where no additional processes become accessible, the fractions only gradually change, eventually approaching reasonably constant values at E 1–10 keV. For processes other than heating, as the ionisation fraction increases, the cross-section decreases, lowering the amount of neutral hydrogen until the heating fraction is equal to one. The background gas is thought to have a density in this study that is equivalent to the cosmic mean at $z = 10$. The interaction rates all scale linearly with the absolute density, so the results are roughly independent of it. As only fixed discrete ionization fractions and energies are tracked, for values between them they advocate to interpolate the exact results. The plots below show interpolation using linear approach and cubic approach.

Visually there were not a lot of difference between the two approaches, except for the region between 0.1 and 0.5 ionization fractions. For simplicity and computational efficiency linear interpolation will be used. After a thorough analysis if need be then the cubic interpolation will be incorporated instead.

4.4 Ionization field

To calculate the X-Ray heating, one also needs the value of the neutral fraction of each cell. The ReionYuga simulation calculates the neutral fraction using excursion-set formalism. This is accomplished by comparing the amount of neutral hydrogen with the amount of ionizing photons available. This comparison is performed on several smoothing scales, starting from the cell size to a sphere corresponding to 20 Mpc (the mean free path of UV photons). This simulation doesn't take into account the inhomogeneous recombinations taking place in the clumpy IGM. The figure below 4.4 shows the ionization field at redshift z = 10.1.

4.5 X-Ray Heating Formalism

Having described all the small steps to calculate the required quantities and fields, it is now to bring everything together and describe the formalism that will be used to incorporate all of this in to a single self-consistent simulation. The final heating per baryon is calculated by culminating all the above equations (Note that heating per baryon is calculated instead of heating rate per baryon as the dt derivative gets absorbed in eq 2.9),

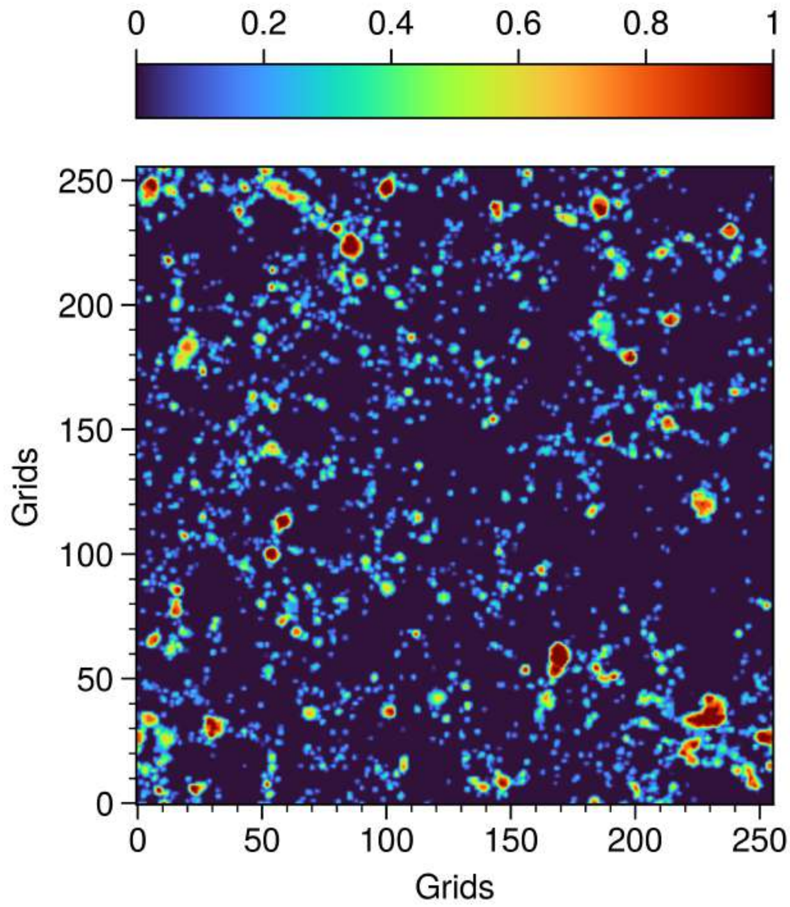

Figure 4.4: Ionization field at redshift z = 10.1. Mass average ionization fraction $x_i = 0.128$.

$$\epsilon_x = (1+z)^4 \, \frac{L_0 c}{h\nu_0} \, N_X \int_{\nu_0}^{\nu_{max}} dv \left(\frac{\nu}{\nu_0}\right)^{-\alpha-1} \sum_i (h\nu - E_i^{th}) \, f_{heat} \, f_i \, x_i \, \sigma_{\nu,i} \int_z^{\infty} dz' \left(\frac{dM_h}{dz'}\right) \frac{1}{H(z')} \frac{1}{(1+z')^2} \tag{4.8}$$

Here there are two integrals which are independent of each other and hence can be calculated separately.

4.5.1 Integral over Redshift

The first thing one needs to calculate this integral is to know how far back in redshift does one need to consider. This can be calculated by taking the mean free path X-rays into account. In this simulation the value of mean free path is taken to be equal to the length of the box i.e 143.36 cMpc in this case. The figure below 4.5 shows the formalism used to calculate this integral.

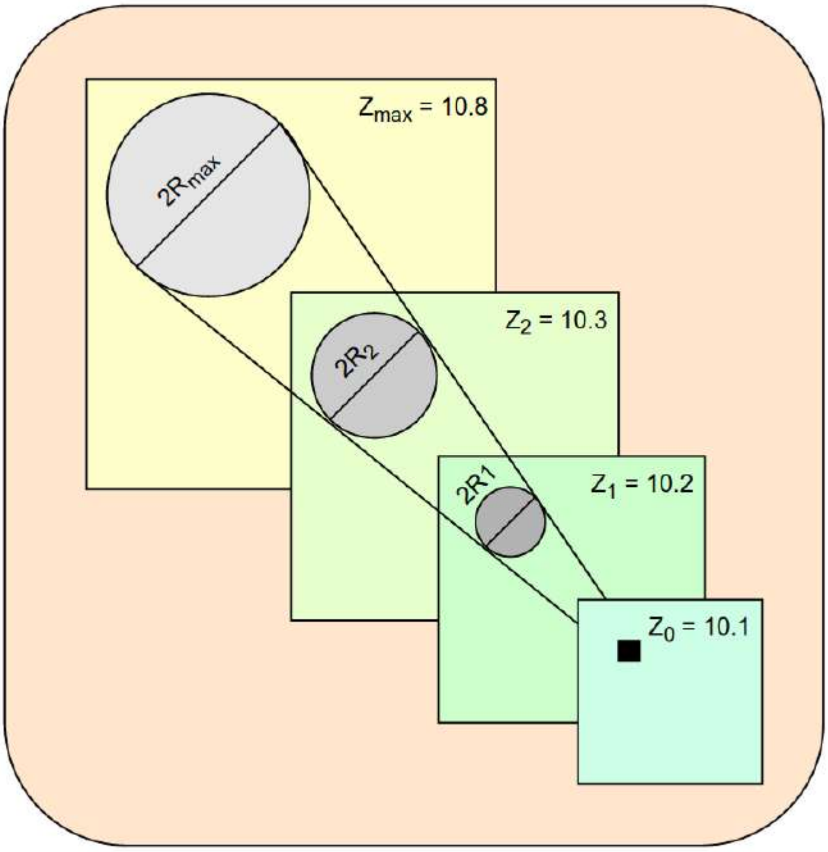

Figure 4.5: X-ray heating formalism

Suppose the heating per baryon is to be calculated for redshift $z = 10.1$. Consider the value to be calculated for the cell shown in the Fig. 4.6. Since light has a finite time travel not all the halo of the previous redshifts will be able to contribute, so one needs to take the lightcone into consideration. So for redshift $z = 10.1$, taking into account a mean free path of 143.36 Mpc, one needs to go back till redshift $z = 10.79 \approx 10.8$. The gap between two redshifts of 0.1 is arbitrary and not inspired by any mathematical calculations. For each redshift the corresponding value of Radius is calculated using the equality as shown below, and then the field is smoothed using a spherical filter with that radius. Using this formalism the finite light time travel is taken into consideration along with the contributions from past density fields.

$$\frac{dR_1}{dt(z = z_1)} = \frac{dR_2}{dt(z = z_2)} = c \tag{4.9}$$

The figure below (Fig. 4.8) shows the values of smoothing radius R (cMpc) corresponding to each redshift using the above equation. Here the lowest value corresponds to the cell length which 0.07 cMpc.

Now that the redshift values to be integrated are known, the next

```
z : 10.100000
R : 0.070000
z : 10.200000
R : 21.484447
z : 10.300000
R : 42.613377
z : 10.400000
R : 63.462673
z : 10.500000
R : 84.038834
z : 10.600000
R : 104.347572
z : 10.700000
R : 124.394432
z : 10.800000
R : 143.360001
```

Figure 4.6: Smoothing radii for different redshift values

thing to calculate is the Hubble function which directly comes from the cosmological model taken into consideration, in this case the standard $\Lambda - CDM$ model is considered. The only thing left to calculate is the derivative of mass of halo with respect to redshift. From the FoF code, the halo catalogs are known i.e the values of M_h are known. The differential is calculated using the first principle,

$$\frac{dM_h}{dz} = \frac{M_h(z-h) - M_h(z+h)}{2h} \tag{4.10}$$

where h = 0.1 as mentioned previously. The integral is then converted to a summation as the snapshots are only available for certain discrete redshifts.

4.5.2 Integral over Frequency

As mentioned in sec. 4.3, the value of heating fraction is known only for 14 values of ionization fraction, for the values in between one needs to interpolate the integral. So, for those 14 values the integral can be pre-calculated before the simulation starts. The integral is performed using Gauss–Kronrod quadrature formula, an adaptive method for numerical integration. For this case as the function is smooth, a 15-point Gauss-Kronrod rule can be used which will provide better accuracy. The GSL compiler has an inbuilt function for calculating this. Once the integral is calculated it can be then interpolated according to the ionization fraction of each cell (sec. 4.4). The values of both the integrals is then be multiplied along with the prefactors to get the final heating per baryon field.

4.6 Effects of previous density fields

The photon flux field is shown below (Fig. 4.7, the values are in terms of per unit solar mass and per unit Mpc. Note that the prefactors in eq. 4.8 are not yet multiplied for simplicity, this will be implemented in the next section. This look quite similar to those of the halo map which shown before (Fig. 4.2), the change is the intensity of the points but overall the features remain the same. This is because the ingredient field that is the halo itself doesn't change over this time period. The bottom figure (Fig. 4.8) show the halo map at redshift $z = 10.8$ which is the furthest redshift that was considered. Comparing these two, one can see that the features are more or less the same, only the value of intensity has changed.

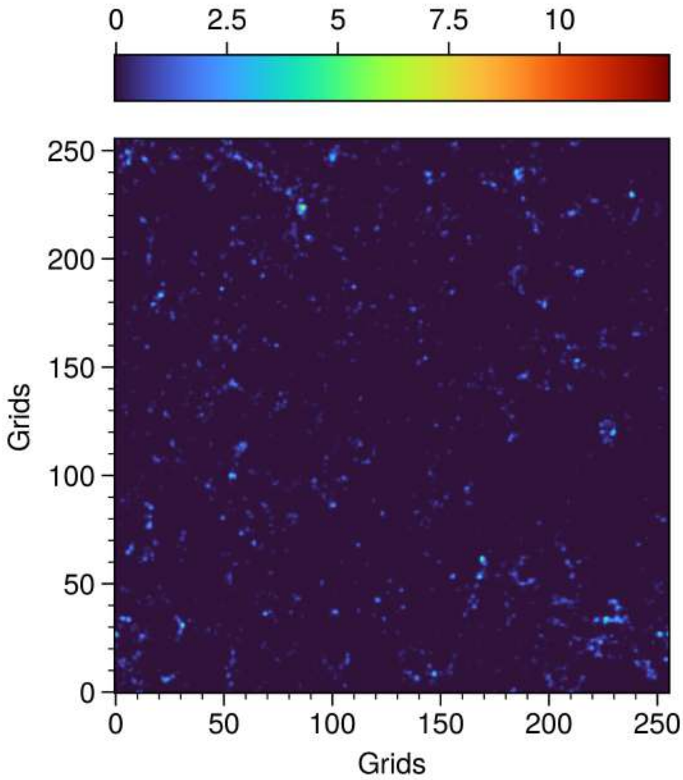

Figure 4.7: Photon number flux field ($z = 10.1$)

From the differential field it is visible that the features are the same, only the intensity changes i.e over-dense regions become more over-dense and under-dense regions become more under-dense. The next thing to analyze is the effect of taking the previous redshift density fields into consideration while calculating the photon number flux field and which in turns forms the heating field. Fig. 4.9 shows the difference between considering just the present density field ($z = 10.1$) and taking both the current and the redshift just before it ($z = 10.2$).

Comparing this with the total photon flux field (Fig. 4.8), one can see that taking the redshift just prior to the present has an

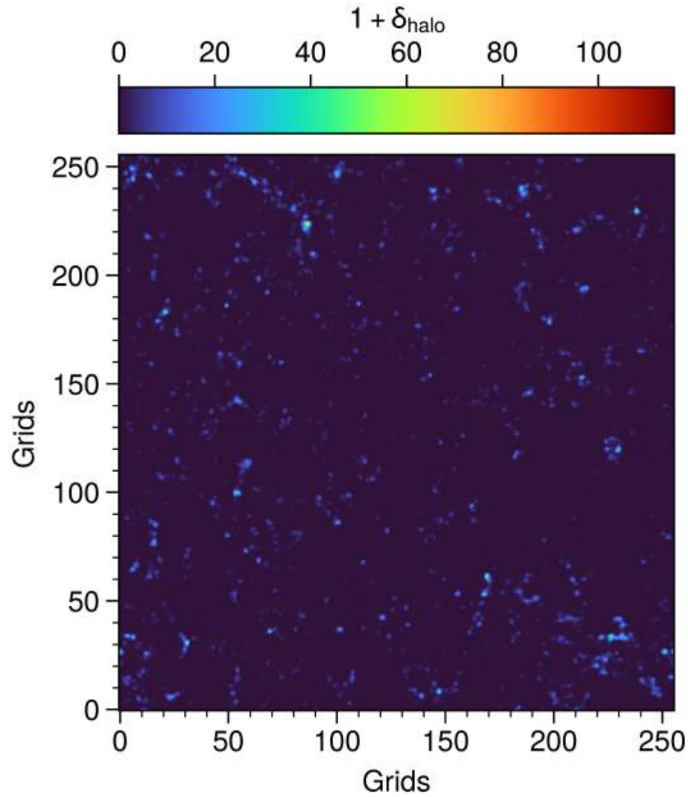

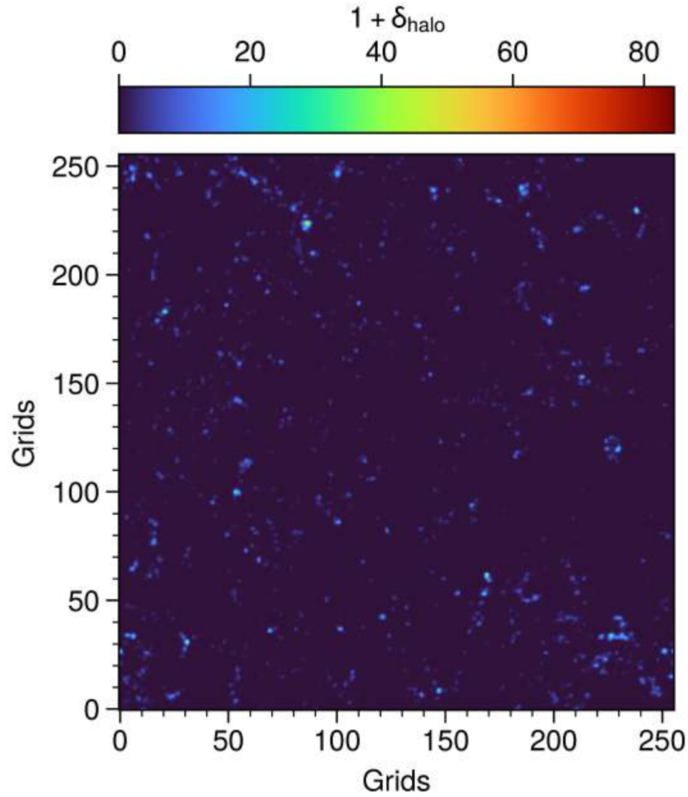

Figure 4.8: Halo density field Top : $(z = 10.1)$ Bottom : $(z = 10.8)$

impact of around 60%. Now if all the prior redshifts are considered from $z = 10.2$ to $z = 10.8$ the difference is very small. Fig. 4.10 shows the difference between considering just $z = 10.1,\ 10.2$ and

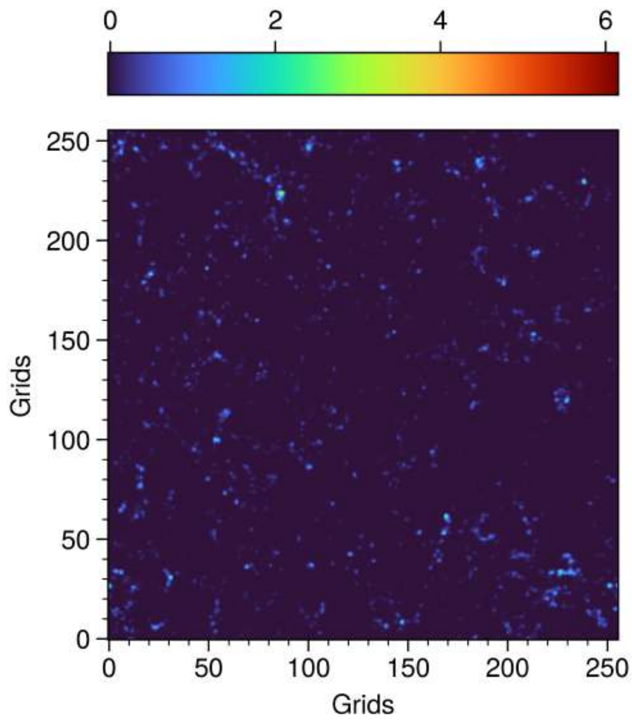

Figure 4.9: Difference in photon number flux field between considering just ($z = 10.1$) and considering both($z = 10.1 + z = 10.2$) Halo density field.

considering all the redshifts.

This is only 0.3% of the original photon number flux field (Fig. 4.7). This is because as seen in Fig. 4.6 the smoothing radius increases as one goes back in redshift, hence after smoothing with such large radii (greater than order 2 compared to the cell size which corresponds to order of 7 difference in volume) the value at each cell becomes very low and saturates after a point. Fig. 4.11 shows the value of the density at each redshift after smoothing the field. As is evident, the density becomes very low after smoothing and doesn't change much after that. This in turn affects the photon number flux as this depends on the change in the density field (Fig. 4.12). Here the value of redshift depicts the redshift till which the contribution is taken.

The heating per baryon after multiplying the frequency integral to the photon number flux is shown in Fig. 4.13. Again, this looks quite similar to that of the photon number flux (Fig. 4.8)as the frequency integral doesn't add any new feature but changes the intensity of the points.

4.7 Logarithmically spaced snapshots

From the previous section it was clear that the snapshots closer to the present redshift contribute more to the photon flux and thus to

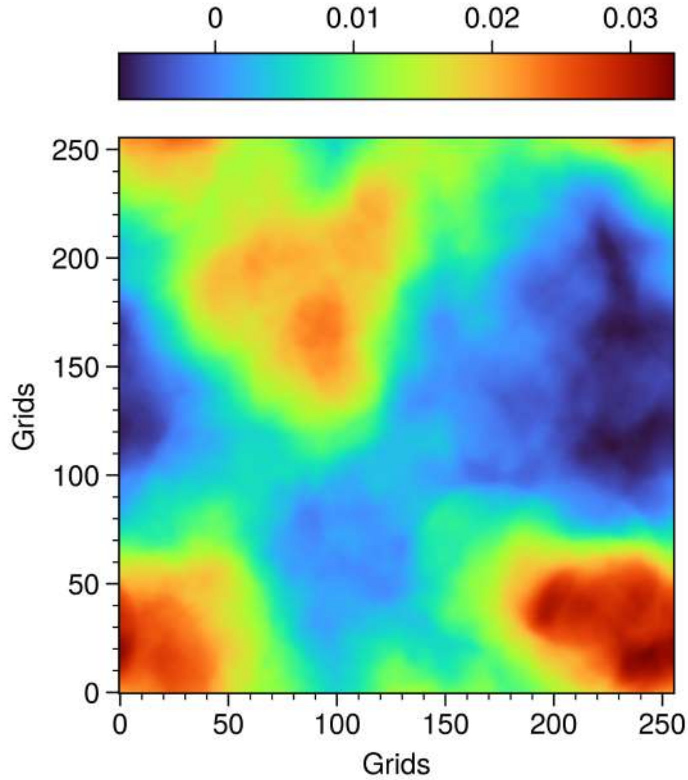

Figure 4.10: Difference in photon number flux field between considering just ($z = 10.1,\ 10.2$) and considering all the Halo density field.

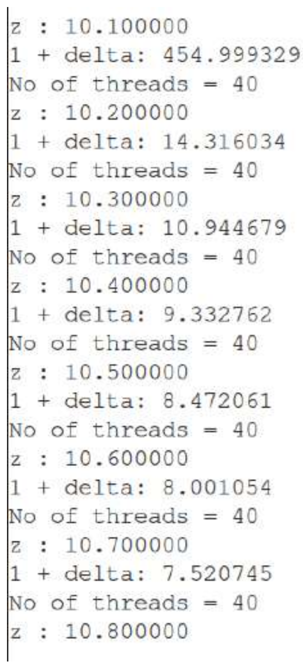

```
z : 10.100000
1 + delta: 454.999329
No of threads = 40
z : 10.200000
1 + delta: 14.316034
No of threads = 40
z : 10.300000
1 + delta: 10.944679
No of threads = 40
z : 10.400000
1 + delta: 9.332762
No of threads = 40
z : 10.500000
1 + delta: 8.472061
No of threads = 40
z : 10.600000
1 + delta: 8.001054
No of threads = 40
z : 10.700000
1 + delta: 7.520745
No of threads = 40
z : 10.800000
```

Figure 4.11: Value of smoothed density field at a particular cell for different redshifts.

the heating field. In 21cmFAST, the snapshots considered between

```
Redshift : 10.100000
Photon number flux : 1.283836
Phi map written
Redshift : 10.200000
Photon number flux : 2.304492
Phi map written
Redshift : 10.300000
Photon number flux : 2.315595
Phi map written
Redshift : 10.400000
Photon number flux : 2.320937
Phi map written
Redshift : 10.500000
Photon number flux : 2.323728
Phi map written
Redshift : 10.600000
Photon number flux : 2.325662
Phi map written
Redshift : 10.700000
Photon number flux : 2.327654
Phi map written
heating map written
```

Figure 4.12: Value of cumulative photon number flux at a particular cell due to contribution from prior redshifts.

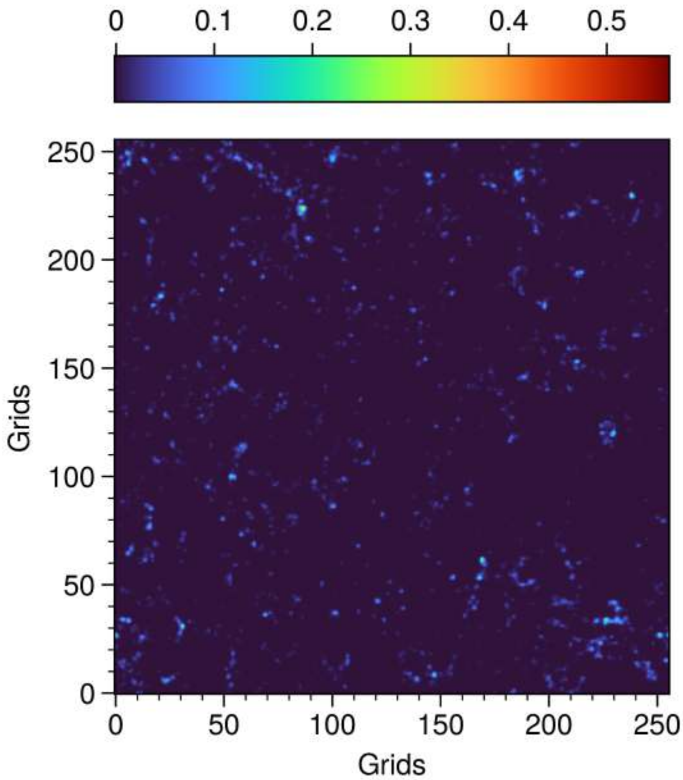

Figure 4.13: Heating per baryon field ($z = 10.1$)

the present and the farthest redshifts are spaced in a logarithmic fashion with more snapshots closer the present redshift is considered. Fig. 4.14 shows the redshifts considered when z=10.247 is the present redshift.

```
z : 10.247167
z : 10.247369
z : 10.247445
z : 10.247540
z : 10.247652
z : 10.247789
z : 10.247954
z : 10.248155
z : 10.248397
z : 10.248692
z : 10.249046
z : 10.249476
z : 10.249997
z : 10.250628
z : 10.251390
z : 10.252312
z : 10.253428
z : 10.254779
z : 10.256413
z : 10.258391
z : 10.260786
z : 10.263684
z : 10.267194
z : 10.271441
z : 10.276584
z : 10.282810
z : 10.290351
z : 10.299484
z : 10.310549
z : 10.323956
z : 10.340209
z : 10.359918
z : 10.383826
z : 10.412848
z : 10.448101
z : 10.490955
z : 10.543102
z : 10.606633
z : 10.684146
z : 10.778885
```

Figure 4.14: Redshift variation ($z_0 = 10.247$)

As one can see there are lots of redshifts now closer to the present redshift. Now the issue is that one can't have snapshots of the density field so close to each other and even then having 40 snapshots within a span of 0.5 redshift is computationally heavy. Hence, we use the closest snapshot that is available to that redshift. Considering this approach and taking into account all the prefactors, following is the resulting photon field 4.15. Note that the units are in per Mpc and per solar mass.

One can now see the smoothing effects around the halos which was previously missing. Even though there voids present in between the halos, the photon field doesn't go to zero as it was the case in the previous prescription.

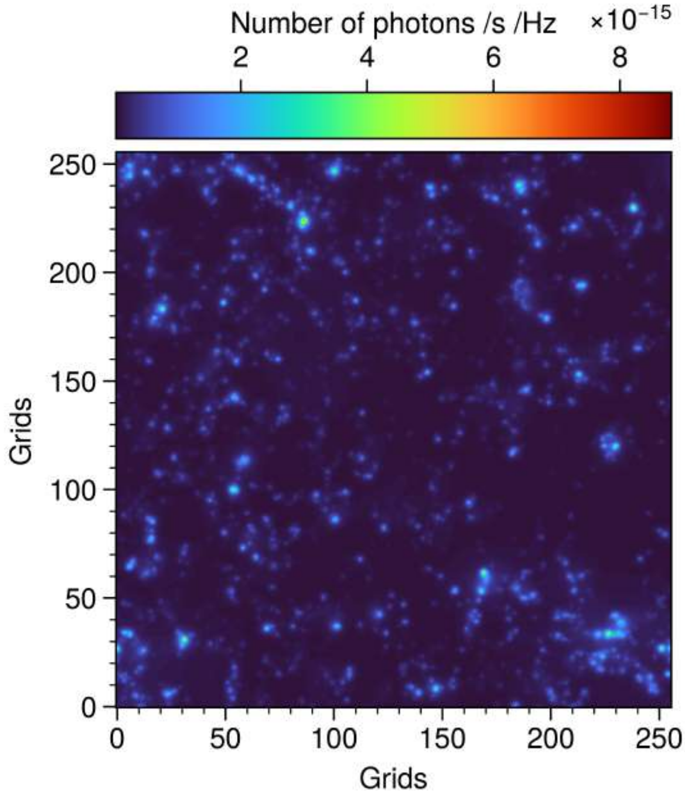

Figure 4.15: X-Ray photon flux field at $z = 10.247$

Chapter 5

Impact of Halos on the Photon Flux Field

After implementing the above mentioned formalism the next natural step is to conduct some statistical analysis to quantify the improvements implemented. To achieve this we first made a mock version of the 21cmFAST (called N-Body_cmfast now onwards), which uses the same heating formalism as it has been implemented in their source code. This is then compared with the formalism mentioned in sec. 4.5 which uses the Halo field to calculate the heating field. In both the cases the density field used is the same , which is created using PM N-Body code. Halos are then identified using a Friend-of-Friends algorithm (Fig. 5.1).

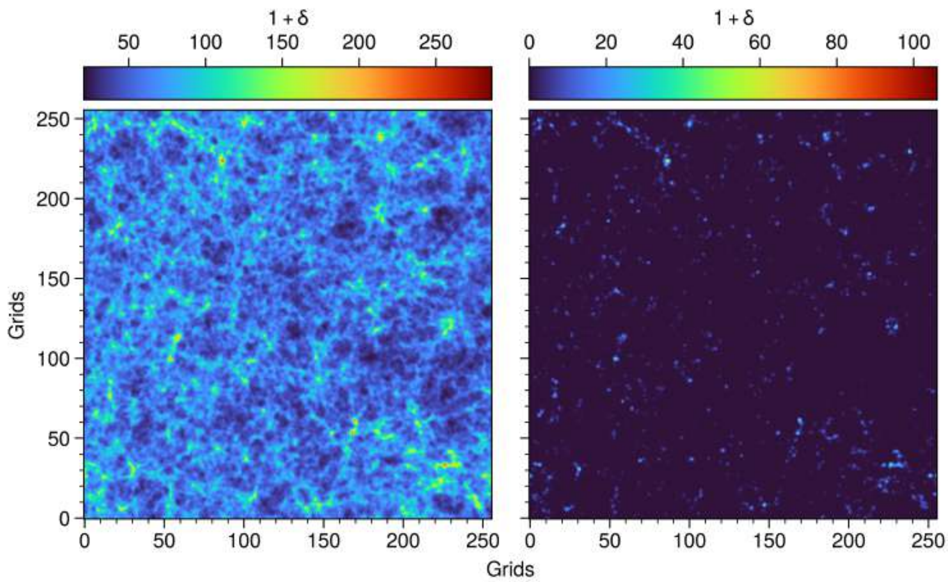

Figure 5.1: Density fields at $z = 10.247$ Left : Dark Matter Right : Halo

5.1 N-Body_cmfast

To calculate the photon flux one needs the SFD as shown in 4.1. The SFD is in turn calculated using 4.6. As 21cmFAST doesn't identify halos it instead calculates the collapsed fraction using the Sheth-Tormen formalism. This is an analytic formalism imposed on the density field instead of identifying the halos to calculate the collapsed fraction. So in the mock case as well we go with the same formalism and implement all the equation as it was done in 21cmFAST. Fig. 5.1 shows the resulting flux field obtained using this formalism. Note that the values are in the units of per Mpc and per solar mass.

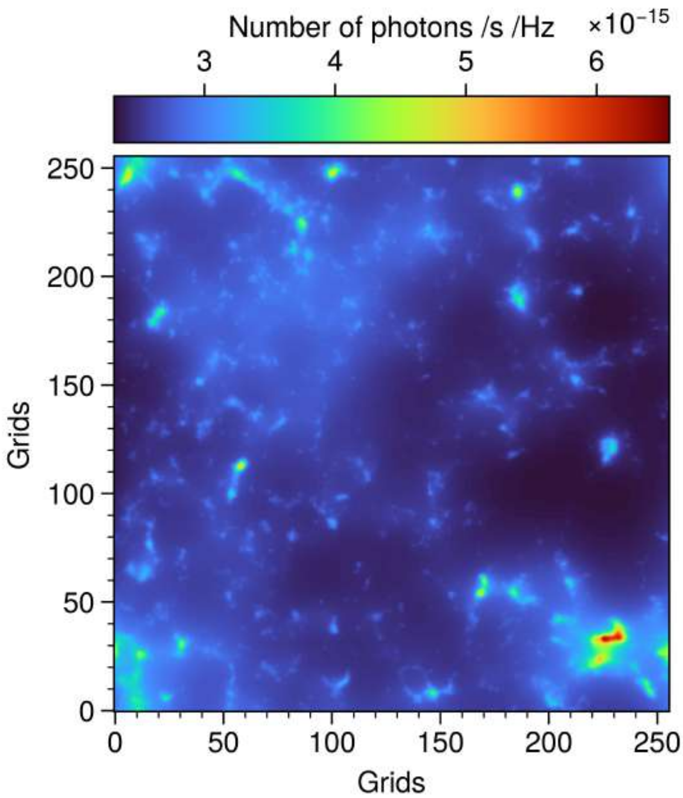

Figure 5.2: X-Ray photon flux field at $z = 10.247$ for mock 21cm-FAST

From the plot one can deduce that in the Nbody_cmfast case the photon field looks much more dispersed as compared to that of the halo case (4.15). This is because the halos are concentrated discrete objects and as a result the photons generated from such a field will also be discrete. Also, there are voids in the halo case wherein the photon flux reaches close to zero which is not seen in the Nbody_cmfast case.

5.2 Statistical Analysis

One needs to perform some kind of analysis to quantitatively measure the impact of using the halos. Fig. 5.3 shows the photon flux field at four different redshifts ($z = 18.332, 14.526, 9.482, 5.727$). From the side by side comparison one can see that, first the halo case looks like a concentrated version of the NBody_cmfast case. Secondly the dynamic scale for both the maps are more or less the same, this is because the photon production efficiency is the same for both the cases. At higher redshift (i.e $z = 19.057$) number of halos formed are very low as a result the derived photon field also has only a few sites of photon production.

In the first subsection 5.2.1, we will check the total photon flux for both the cases at different redshifts. In the second subsection 5.2.2 we will discuss a special case wherein we increase the photon production efficiency. Then in the third subsection 5.2.3, the histogram of the photon field will be analysed. In the final subsection 5.2.4, the power spectrum for all the cases will be plotted.

5.2.1 Total photon flux

Table 5.1 shows the total photon flux for both the cases. As one would have expected from the figures above, the total flux for the Nbody_cmfast is much greater than that of the halo. This is because in the prior case, all of the collapsed objects produce X-ray photons, whereas in the latter case only the halos produce the photons. The fourth column shows the ratio of the total photon flux. As the redshift increases more and more halos form, as result the total photon flux for the halo case increases, thus the ratio decreases with redshift.

z	Total flux : Nbody_cmfast	Total flux : Halo	Ratio
18.332	4.6059517e-10	5.3154863e-12	86.65
14.526	7.519879e-09	1.5585797e-10	48.25
9.482	5.3761976e-08	4.313012e-09	12.46
5.727	4.5788056e-08	1.9647374e-08	2.33

Table 5.1: Total Photon Flux.

5.2.2 Boosted Photon Production

To overcome this lack of photons in the Halo approach, one option is to increase the photon production efficiency parameter Nx (Taken to be 54 in this case, which makes the total photon flux ratio to be close to 1 at $z = 14.526$). Rest of the formalism remains the same. Fig. 5.4 shows the photon flux map for the boosted photon production (BPP) case. As one can see, now the halos are emitting

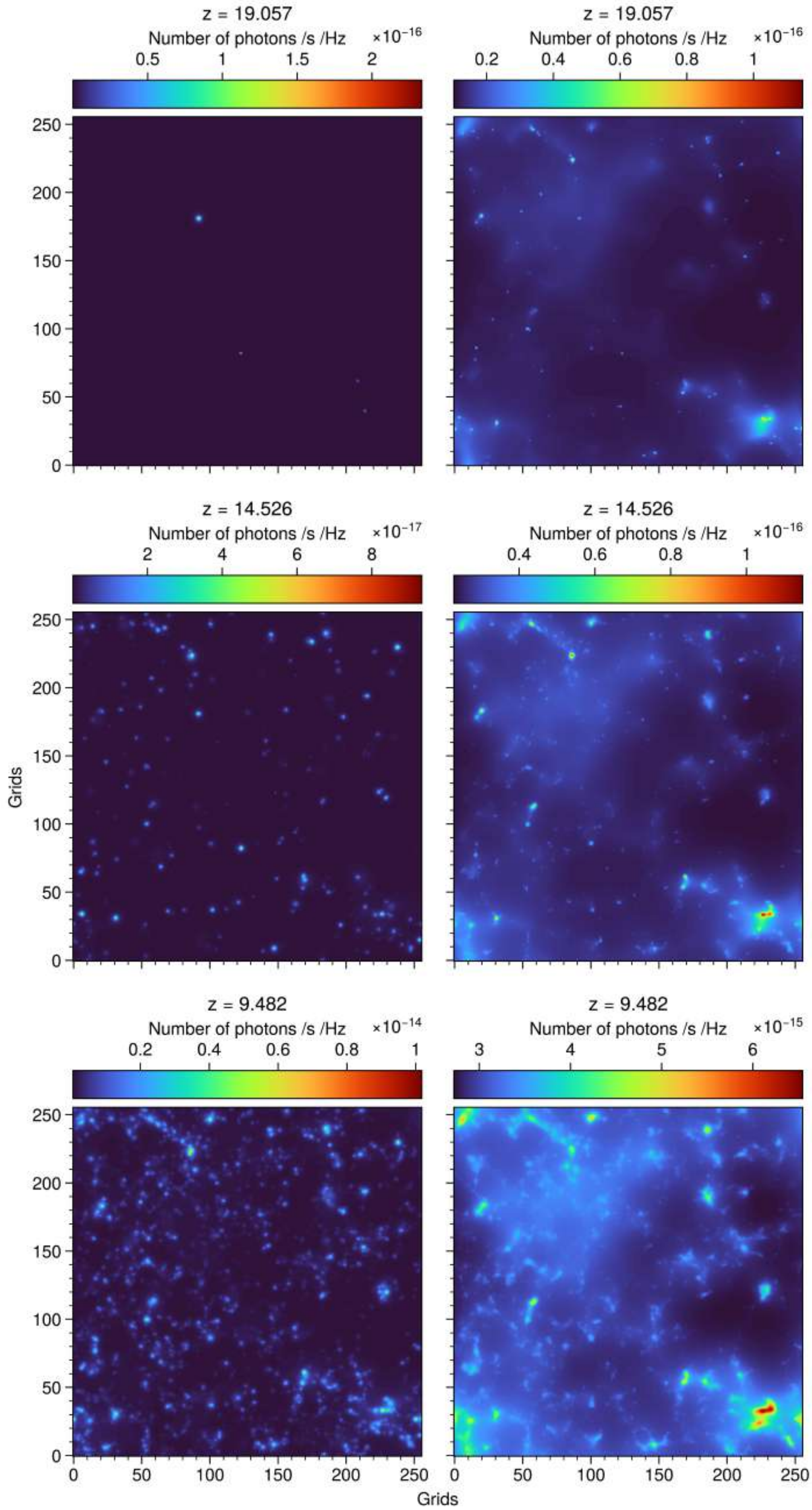

Figure 5.3: X-Ray photon flux field at $z = 18.332, 14.526, 9.482, 5.727$ top to bottom. Left : Halo Right : NBody_cmfast

a lot more photons as compared to Fig. 4.15. Table 5.2 shows the total photon flux at different redshifts.

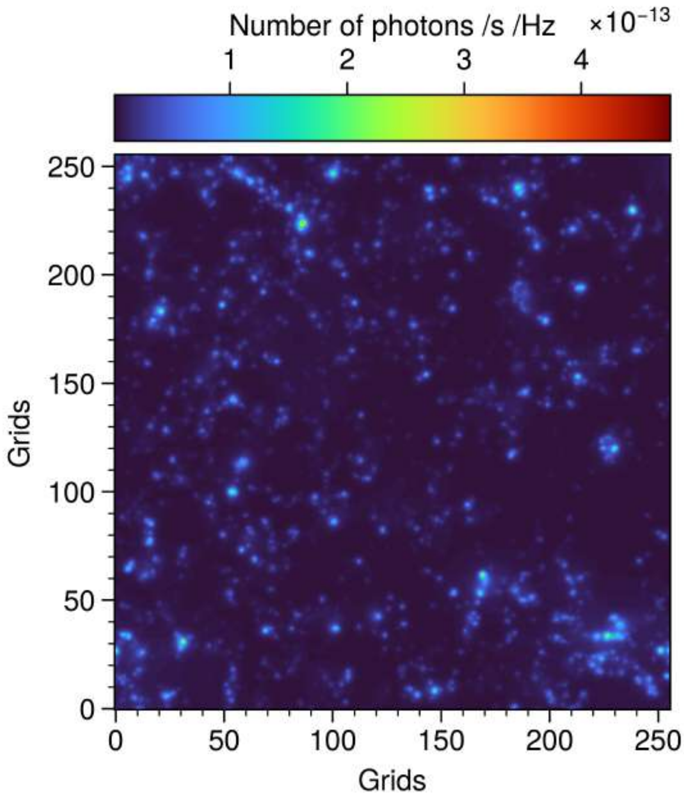

Figure 5.4: X-Ray photon flux field at $z = 10.247$ for BPP

z	Total flux : Nbody_cmfast	Total flux : BPP	Ratio
18.332	2.4144742e-10	2.8772912e-10	1.6
14.526	4.8432874e-10	5.2374943e-10	0.925
9.482	5.3761976e-08	2.3290299e-07	0.23
5.727	6.8061974e-09	1.0609576e-06	6.4e-3

Table 5.2: Total Photon Flux BPP.

From the table one can conclude that taking a constant Nx for all the redshifts is not an ideal scenario, since even though the ratio becomes close to one at $z = 14.526$ at other redshift this result is not found. At higher redshift the value of Nx underestimates while at lower redshift it overestimates the number of photon production.

5.2.3 Histogram

Fig. 5.5 shows the histogram of the number of pixels in certain flux bins. The flux values in the Nbody_cmfast case is concentrated in a few bins whereas the Halo case is spreaded out throughout a wider dynamic range. This is because at the lower end, the halo photon field goes to close to zero values as there are lots of pixels where halos are not present. At the extreme end, since the halo are concentrated objects the biggest halos end up producing a large photon flux. In between since there are discrete halos present in this range, there is a spread observed in the histogram as well.

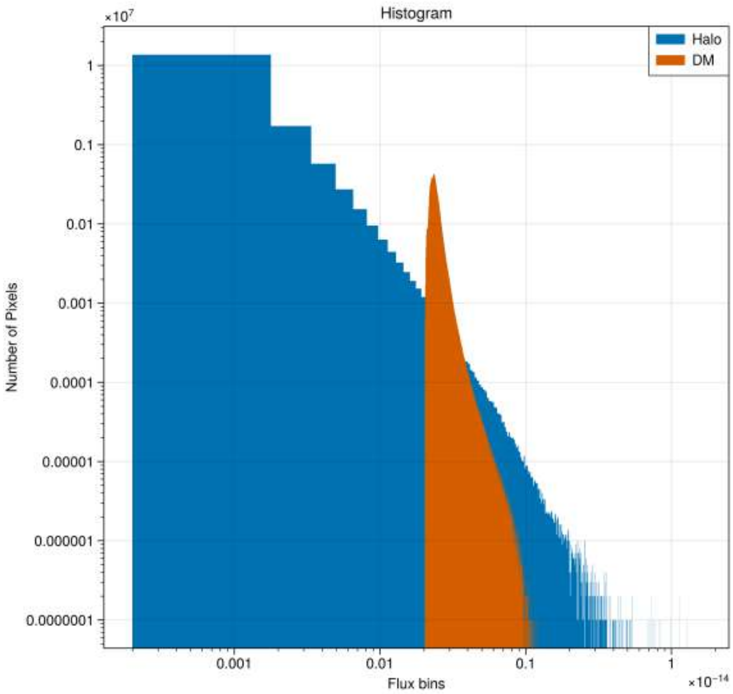

Figure 5.5: Histogram of the number of pixels in certain flux bins

5.2.4 Power spectrum

For the final analysis we show the power spectrum for both the photon flux fields Fig. 5.6. At large length scales i.e low k values the total photon flux dominates. Hence except for the last the redshift, the power for Nbody_ cmfast case is higher than that of the Halo. At lower length scales i.e high k values the small scale feature dominate. Since halos are concentrated objects they will dominate at this scale given that halos are present. At higher redshifts since not much halos are formed the power for Nbody_ cmfast case is higher, but as redshift decreases more and more halos form and thus the power for the halo case croses above Nbody_ cmfast.

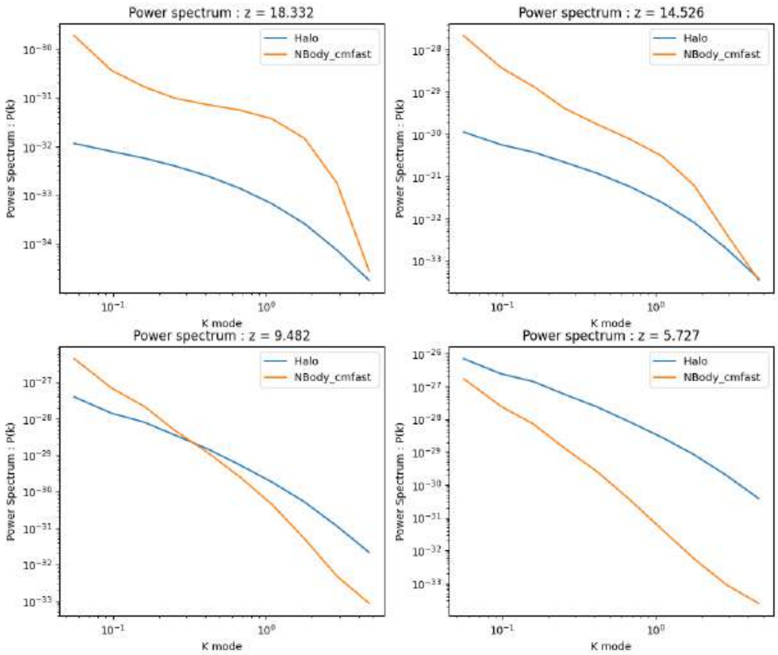

Figure 5.6: Power Spectrun : Photon flux fields at $z = 18.332, 14.526, 9.482, 5.727$ for both the cases.

Chapter 6

IGM Temperature Evolution

Now that we have the required photon fields and the heating field we can use these as ingredient fields along with the matter fields to calculate the kinetic temperature evolution using eq. 2.9. This will in turn be used along with the color temperature to calculate the spin temperature (eq. 2.1). Finally we will calculate the brightness temperature using eq. 1.2. The same processes will be repeacted for N-Body_cmfast case as well. After getting these fields for both the cases, statistical analysis will be performed to analyse the difference between the two approaches.

6.1 Kinetic Temperature

To get the kinetic temperature (T_k) of the IGM at a particular redshift, one needs to know T_k at the previous redshift i.e kinetic temperature is a cumulative quantity. Eq. 2.9 shows the T_k evolution with redshift. This equation has three components viz., Heating due to various astrophysical processes (in this case X-ray heating and compton heating are considered 2.6), Adiabatic cooling due to expansion of the universe and last term corresponds to change in the ionization state of the IGM. Out of these three components only the first term leads to an increase in the kinetic temperature. Since T_k is an evolved quantity one needs a value to start the evolution at a high redshift. For this we use RECFAST (Seager et al. (1999)) code which provides us with initial condition for T_K and x_e. In our case we start at an intial redshift of $z = 22.254$ when the first halos start forming, and then we evolve eq. 2.9 till redshift $z = 5.727$, when re-ionization is supposed to have ended.

6.1.1 Evolution with redshift

Fig 6.1 shows the kinetic temperature map obtained by evolving eq. 2.9. The map is shown at four different redshift viz. $z = 18.332, 14.526, 9.482, 5.727$ for both the approaches. As the redshift decreases the temperature seems to be increasing. At the final redshift the kinetic temperature for the halo case reach very high values comparatively. The maps become more and more concentrated as the redshift decrease. This is because the ingredient matter density field itself becomes more concentrated due to gravity.

6.1.2 Power Spectrum

Fig. 6.2 shows the power spectrum for both the cases at four different redshifts. The redshift trend followed by Power spectrum is similar to that of the Phi power spectrum (sec. 5.2.4)

6.2 Spin Temperature

Spin temperature depends on three parameters viz. Kinetic Temperature, Color Temperature and Background radiation temperature. In the previous section we had calculated the kinetic temperature, and the radiation temperature is the CMB temperature which depends only on redshift, hence it is straight forward to calculate it. The only thing remaining is the color temperature, this will be calculated by the prescription mentioned in Hirata (2006). Other then the three temperature parameter there are two coupling factors which are calculated using eq. **??** and eq. 2.6

6.2.1 Evolution with redshift

Fig 6.3 shows the spin temperature map obtained at four different redshift viz. $z = 19.057, 14.526, 9.482, 5.727$ for both the approaches. At the initial redshift the spin temperature is greater for the Nbody_ cmfast case. This may be because there are very halos present at this redshift. As the redshift decreases the spin temperature seems to be decreasing and then increasing for the Nbody_ cmfast case. Whereas in the halo case the spin temperature seems to be increasing with decreasing redshift. At the final redshift the spin temperature for the halo case reach very high values comparatively.

6.2.2 Power Spectrum

Fig. 6.4 shows the power spectrum for both the cases at four different redshifts. The redshift trend followed by Power spectrum is similar to that of the kinetic temperature power spectrum (sec. 6.1.2)

6.3 Brightness Temperature

Once you know the spin temperature, the brightness temperature can be calculated using eq. 1.2. The neutral fraction can be cal-

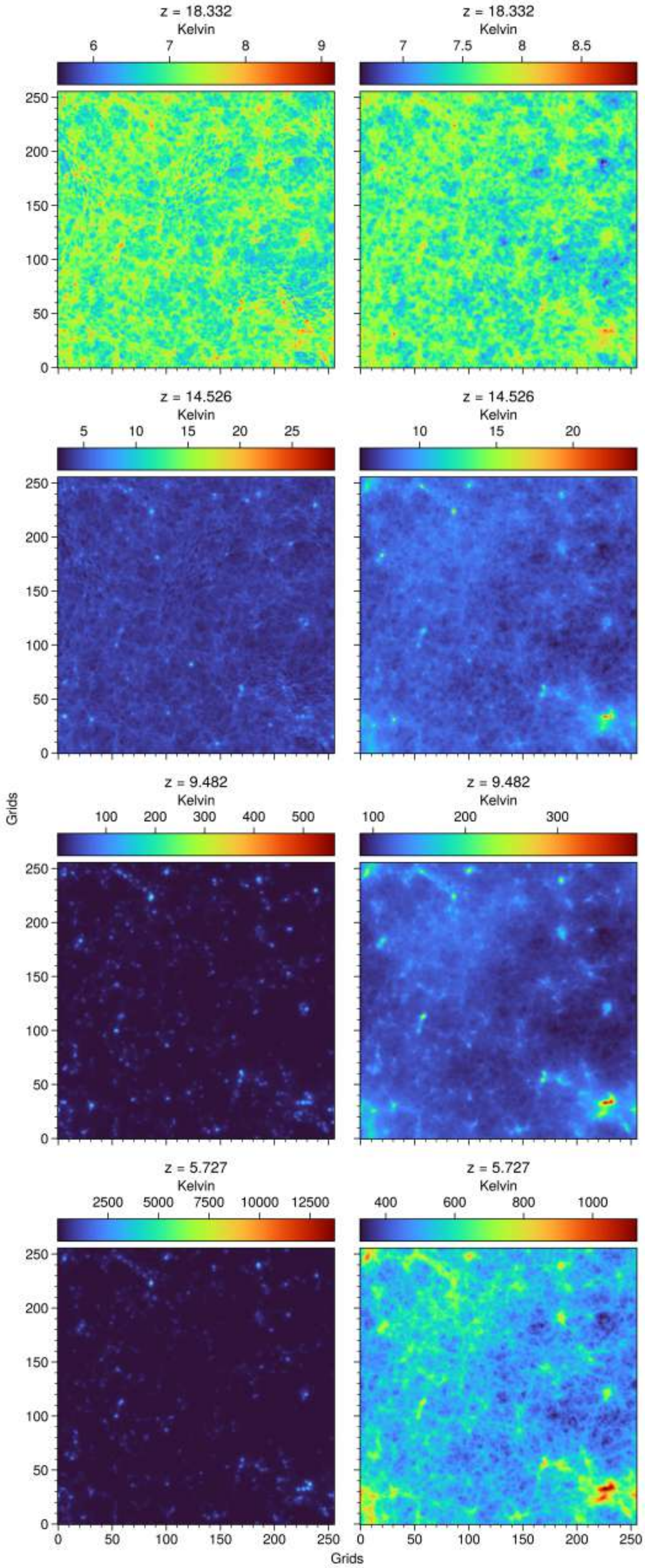

Figure 6.1: Kinetic Temperature maps at $z = 18.332, 14.526, 9.482, 5.727$ top to bottom. Left : Halo Right : Nbody_ cmfast

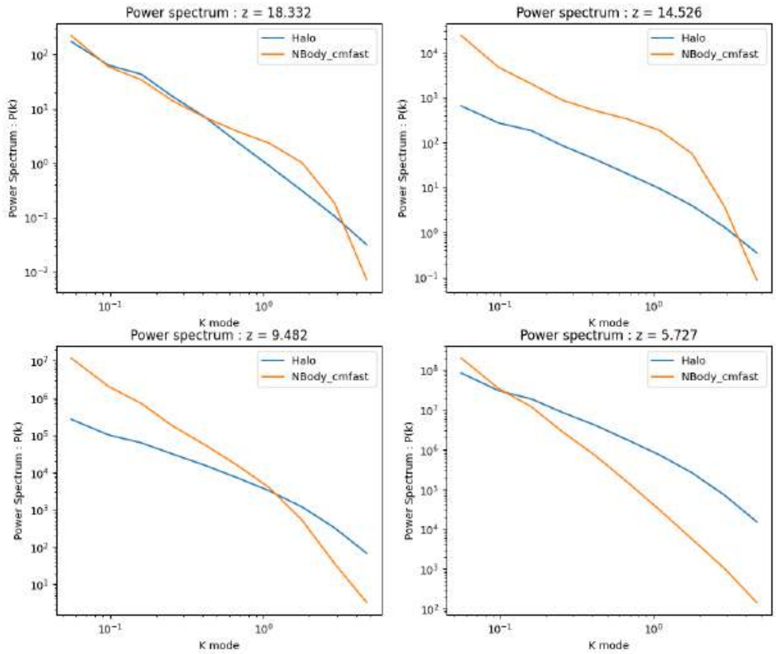

Figure 6.2: Kinetic Temperature Power spectrum at $z = 18.332, 14.526, 9.482, 5.727$ for both the cases

culated easily as we know the ionization fraction from sec. 4.4. In both the cases the the velocity gradient term is assumed to be unity. This will be properly implemented soon.

6.3.1 Evolution with redshift

Fig 6.5 shows the brightness temperature (T_B) map obtained at four different redshift viz. $z = 19.057, 14.526, 9.482, 5.727$ for both the approaches. The brightness temperature for both the maps are pretty different. At lower redshifts, the T_B for Nbody_ cmfast case reaches a positive values whereas the halo case remains negative throughout the redshift evolution. This is because the brightness temperature starts from a very small value and thus when heating begins it is not able to heat the IGM to positive values. The reason why the brightness temperature starts at such low value is because the spin temperature starts at a lower value compared to that of Nbody_ cmfast.

6.3.2 Power Spectrum

Fig. 6.6 shows the power spectrum for both the cases at four different redshifts. At higher redshifts, as mentioned above the brightness temperature is lower for the halo case and the value is negative. As a result the magnitude at higher redshifts will be higher for the halo

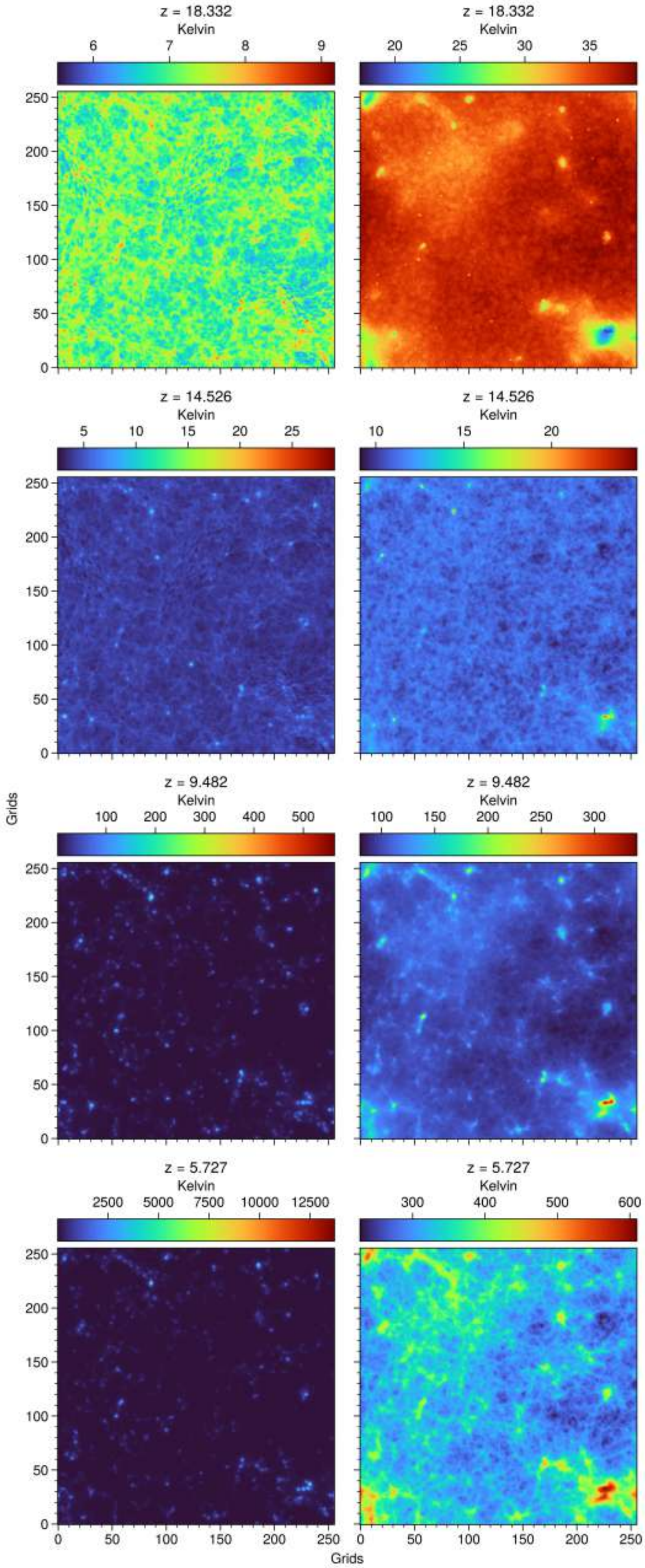

Figure 6.3: Spin Temperature maps at $z = 18.332, 14.526, 9.482, 5.727$ top to bottom. Left : Halo Right : Nbody_ cmfast

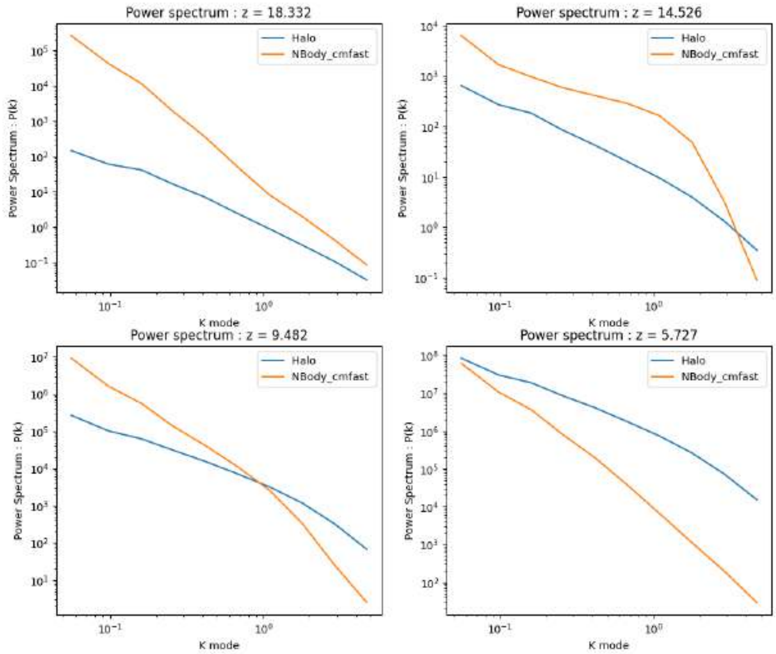

Figure 6.4: Spin Temperature Power spectrum at $z = 18.332, 14.526, 9.482, 5.727$ for both the cases

case. The same can be seen in the power spectrum. As move towards lower redshifts, the value for the Nbody_ cmfast case reaches a positive value while for the halo cases it reaches close to zero. Hence the prior case dominates at low redshifts.

6.4 Mean Temperature Evolution

The figure plotted below shows the evolution of mean kinetic temperature (Fig. 6.7), mean spin temperature (Fig. 6.8) and mean brightness temperature (Fig. 6.9) with redshift. The black dashed line shows the CMB temperature. The plots also show the evolution for the special BPP case (sec. 5.2.2).

Different approaches cross the CMB temperature at different redshift. The BPP case over predicts both the kinetic temperature and the spin temperature. This may be resolved by selecting the Nx parameter such that it varies with redshift and be calibrated to the Nbody_ cmfast.

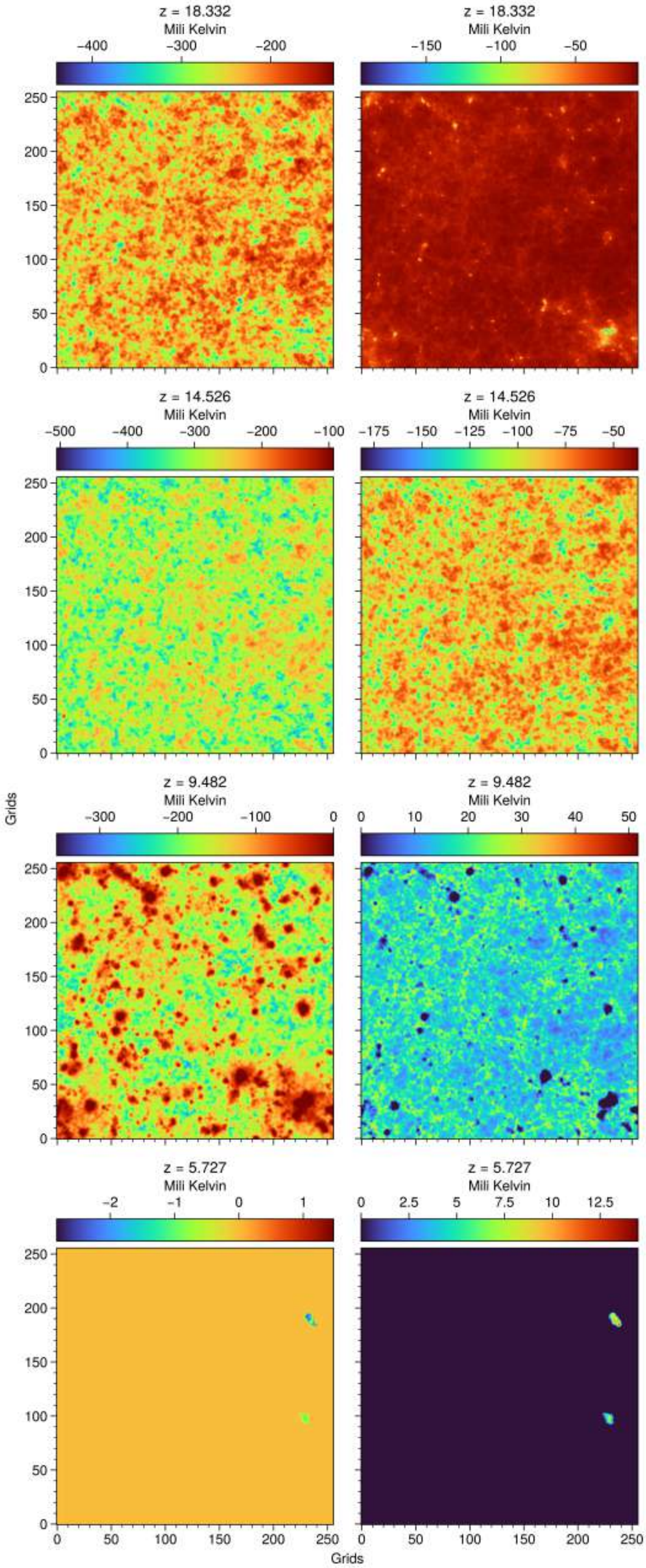

Figure 6.5: Brightness Temperature maps at $z = 18.332, 14.526, 9.482, 5.727$ top to bottom. Left : Halo Right : Nbody_ cmfast

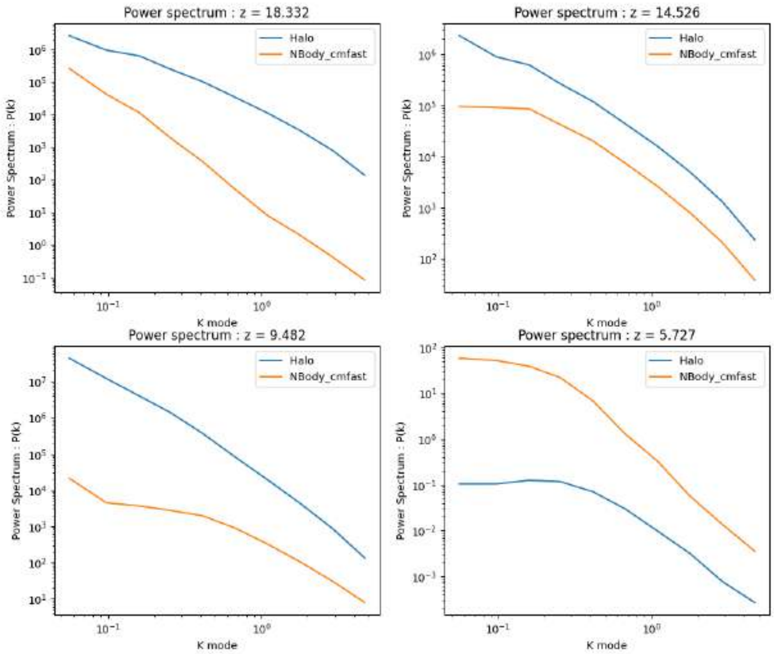

Figure 6.6: Brightness Temperature Power spectrum at $z = 18.332, 14.526, 9.482, 5.727$ for both the cases

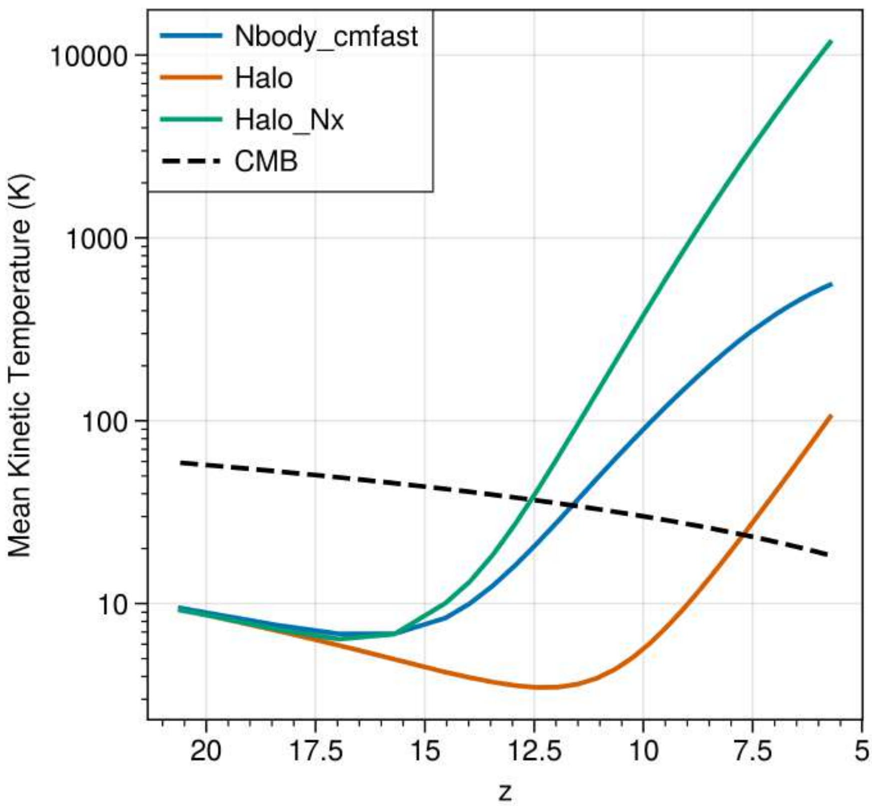

Figure 6.7: Evolution of mean kinetic temperature with redshift for all the cases

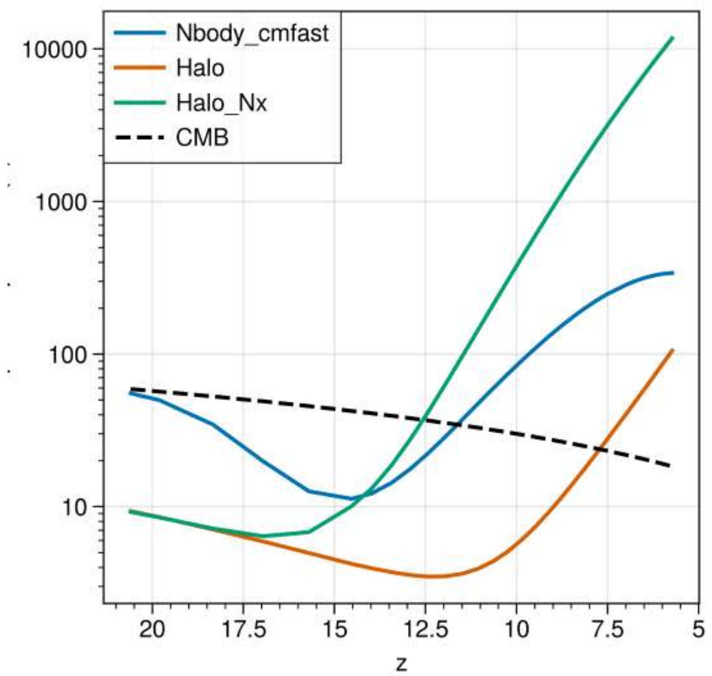

Figure 6.8: Evolution of mean spin temperature with redshift for all the cases

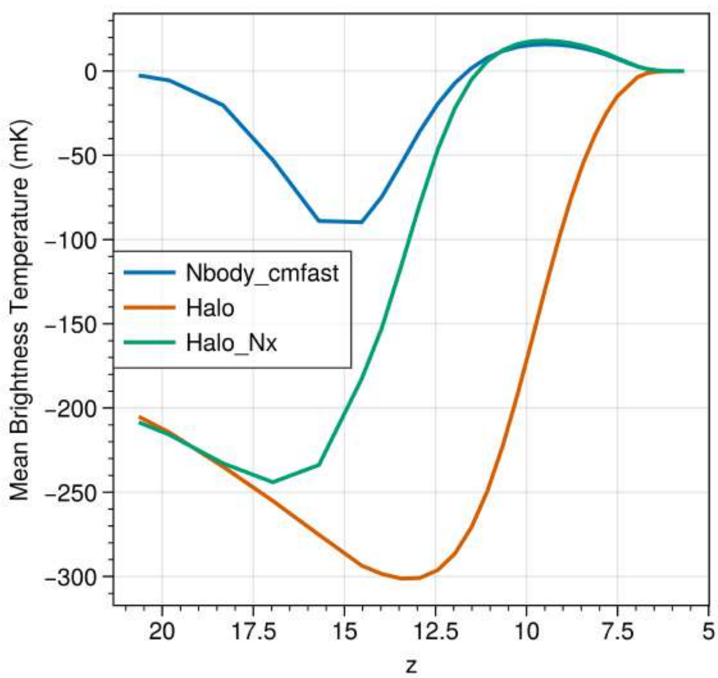

Figure 6.9: Evolution of mean brightness temperature with redshift for all the cases

Chapter 7

Summary and Future work

This thesis introduces a new approach to simulate the cosmic dawn 21cm signal; a combination of high-resolution accurate density fields and a proper treatment of X-ray heating taking the history into consideration. Instead of using Excursion-Set (ES) formalism to identify halo, a friends-of-friend algorithm is used which can identify haloes of all shapes and sizes, unlike the ES method which can identify only spherical halo. This provides more resemblance to the actual universe instead of a toy version of the universe. After creating the halo catalog, for a redshift say $z = 10.1$, the furthest redshift that can affect the present redshift is calculated using the mean free path of X-ray photons (in this case 143.36 Mpc). This is calculated by taking the finite light time travel to account and that the photons traverse on null geodesics. Between the present redshift and furthest redshift density field, intermediate fields are also taken into account with a 0.1 gap in redshift. Keeping the expansion of the universe in consideration, the integrated heating effect is calculated using the photon number flux and source spectral density. Logarithmically spacing the snapshots improves the results drastically. Fig. 4.15 shows the final derived photon flux field.

The N-body takes around 35 minutes to produce a snapshot at each redshift and the FoF then takes around 40 minutes to identify the haloes in each snapshot. The X-ray heating and the ionization formalism then takes around 10 minutes to produce the heating field as well as the ionization field at a particular redshift. All the codes are computed on a local computer with a single processor having 40 cores and 256 GB Ram. From the photon flux field and the ingredient matter fields, the IGM temperature was calculated and evolved throughout the redshift range. There are several difference in both the approach. Using the density matter field instead of the halo field provides more realistic results. Further work needs to be done to investigate the halo approach and find a better prescription. For the coming months, following is a list of work to be done,

- Investigate more on the Halo approach by performing different statistical methods.

- Constrain CD-EoR parameters using fourier or real space statistical analysis.

Bibliography

Alvarez, M. A. (2016). The Kinetic Sunyaev-Zel'dovich Effect from Reionization: Simulated Full-sky Maps at Arcminute Resolution. , 824(2):118.

Barry, N., Wilensky, M., Trott, C. M., and Pindor (2019). Improving the Epoch of Reionization Power Spectrum Results from Murchison Widefield Array Season 1 Observations. , 884(1):1.

Beardsley, A. P., Hazelton, B. J., Sullivan, I. S., and Carroll (2016). First Season MWA EoR Power spectrum Results at Redshift 7. , 833(1):102.

Bharadwaj, S. and Srikant, P. S. (2004). HI fluctuations at large redshifts: III - Simulating the signal expected at GMRT. *Journal of Astrophysics and Astronomy*, 25:67–80.

Chen, X. and Miralda-Escude, J. (2004). The spin–kinetic temperature coupling and the heating rate due to ly scattering before reionization: Predictions for 21 centimeter emission and absorption. *The Astrophysical Journal*, 602(1):1–11.

Choudhury, T. R., Haehnelt, M. G., and Regan, J. (2009). Inside-out or outside-in: the topology of reionization in the photon-starved regime suggested by ly forest data. *Monthly Notices of the Royal Astronomical Society*, 394(2):960–977.

Choudhury, T. R. and Paranjape, A. (2018). Photon number conservation and the large-scale 21 cm power spectrum in seminumerical models of reionization. *Monthly Notices of the Royal Astronomical Society*, 481(3):3821–3837.

Dillon, J. S. and Parsons, A. R. (2016). REDUNDANT ARRAY CONFIGURATIONS FOR 21 cm COSMOLOGY. *The Astrophysical Journal*, 826(2):181.

Field, G. B. (1959). The Time Relaxation of a Resonance-Line Profile. , 129:551.

Furlanetto, S., Zaldarriaga, M., and Hernquist, L. (2004). Statistical probes of reionization with 21 cm tomography. *Astrophys. J.*, 613:16–22.

Furlanetto, S. R. (2007). Spin exchange rates in proton-hydrogen collisions. *Monthly Notices of the Royal Astronomical Society*, 379(1):130–134.

Furlanetto, S. R. and Loeb, A. (2004). Large-scale structure shocks at low and high redshifts. *The Astrophysical Journal*, 611(2):642–654.

Furlanetto, S. R. and Stoever, S. J. (2010). Secondary ionization and heating by fast electrons. *Monthly Notices of the Royal Astronomical Society*.

Gehlot, B. K., Mertens, F. G., Koopmans, L. V. E., and Brentjens (2019). The first power spectrum limit on the 21-cm signal of neutral hydrogen during the Cosmic Dawn at z = 20-25 from LOFAR. , 488(3):4271–4287.

Ghara, R., Mellema, G., Giri, S. K., Choudhury, T. R., Datta, K. K., and Majumdar, S. (2018). Prediction of the 21-cm signal from reionization: comparison between 3d and 1d radiative transfer schemes. *Monthly Notices of the Royal Astronomical Society*, 476(2):1741–1755.

Gnedin, N. Y. and Madau, P. (2022). Modeling cosmic reionization.

Goldenberg, H. M., Kleppner, D., and Ramsey, N. F. (1960). Atomic hydrogen maser. *Phys. Rev. Lett.*, 5:361–362.

Harnois-Deraps, J., Pen, U.-L., Iliev, I. T., Merz, H., Emberson, J. D., and Desjacques, V. (2013). High-performance p3m n-body code: CUBEP3m. *Monthly Notices of the Royal Astronomical Society*, 436(1):540–559.

Hirata, C. M. (2006). Wouthuysen-field coupling strength and application to high-redshift 21-cm radiation. *Monthly Notices of the Royal Astronomical Society*, 367(1):259–274.

Iliev, I., Shapiro, P., Mcdonald, P., Mellema, G., and Pen, U.-L. (2008). The effect of the intergalactic environment on the observability of ly?? emitters during reionization. *Monthly Notices of the Royal Astronomical Society*, 391:63 – 83.

Iliev, I. T. and Mellema (2006). Simulating cosmic reionization at large scales - I. The geometry of reionization. , 369(4):1625–1638.

Jacobs, D., Pober, J., Parsons, A., and Aguirre (2014). Multiredshift limits on the 21 cm power spectrum from paper. *The Astrophysical Journal*, 801.

Kern, N. S., Liu, A., Parsons, A. R., Mesinger, A., and Greig, B. (2017). Emulating simulations of cosmic dawn for 21 cm power spectrum constraints on cosmology, reionization, and x-ray heating. *The Astrophysical Journal*, 848(1):23.

Koopmans, L., Pritchard, J., Mellema, G., Aguirre, J., Ahn, K., Barkana, R., and van Bemmel, I. (2015). The cosmic dawn and epoch of reionisation with SKA. In *Proceedings of Advancing Astrophysics with the Square Kilometre Array — PoS(AASKA14)*. Sissa Medialab.

Liu, A. and Parsons, A. R. (2016). Constraining cosmology and ionization history with combined 21 cm power spectrum and global signal measurements. , 457(2):1864–1877.

Liu, A. and Shaw, J. R. (2020). Data analysis for precision 21 cm cosmology. *Publications of the Astronomical Society of the Pacific*, 132(1012):062001.

Madau, P., Meiksin, A., and Rees, M. J. (1997). 21 centimeter tomography of the intergalactic medium at high redshift. *The Astrophysical Journal*, 475(2):429–444.

Maity, B. and Choudhury, T. R. (2022). Constraining the reionization and thermal history of the universe using a seminumerical photon-conserving code scpscript/scp. *Monthly Notices of the Royal Astronomical Society*, 515(1):617–630.

Majumdar, S., Mellema, G., Datta, K. K., Jensen, H., Choudhury, T. R., Bharadwaj, S., and Friedrich, M. M. (2014). On the use of seminumerical simulations in predicting the 21-cm signal from the epoch of reionization. *Monthly Notices of the Royal Astronomical Society*, 443(4):2843–2861.

Mesinger, A., Furlanetto, S., and Cen, R. (2010). 21cmfast: a fast, seminumerical simulation of the high-redshift 21-cm signal. *Monthly Notices of the Royal Astronomical Society*, 411(2):955–972.

Mondal, R., Bharadwaj, S., and Majumdar, S. (2021). ReionYuga: Epoch of Reionization neutral Hydrogen field generator. Astrophysics Source Code Library, record ascl:2107.005.

Mondal, R., Bharadwaj, S., Majumdar, S., Bera, A., and Acharyya, A. (2015). The effect of non-Gaussianity on error predictions for the Epoch of Reionization (EoR) 21-cm power spectrum. , 449:L41–L45.

Naoz, S. and Barkana, R. (2005). Growth of linear perturbations before the era of the first galaxies. , 362(3):1047–1053.

Paciga, G., Albert, J. G., and Bandura (2013). A simulation-calibrated limit on the H I power spectrum from the GMRT Epoch of Reionization experiment. , 433(1):639–647.

Paciga, G., Chang, T.-C., Gupta, Y., and Nityanada (2011). The GMRT Epoch of Reionization experiment: a new upper limit on the neutral hydrogen power spectrum at z 8.6. *Monthly Notices of the Royal Astronomical Society*, 413(2):1174–1183.

Paranjape, A., Choudhury, T. R., and Padmanabhan, H. (2016). Photon number conserving models of H II bubbles during reionization. , 460(2):1801–1810.

Park, J., Greig, B., and Mesinger, A. (2022). Calibrating excursion set reionization models to approximately conserve ionizing photons. *Monthly Notices of the Royal Astronomical Society*, 517(1):192–200.

Parsons, A. R., Backer, D. C., and Foster (2010). The Precision Array for Probing the Epoch of Re-ionization: Eight Station Results. , 139(4):1468–1480.

Patil, A. H., Yatawatta, S., Koopmans, L. V. E., and de Bruyn (2017). Upper Limits on the 21 cm Epoch of Reionization Power Spectrum from One Night with LOFAR. , 838(1):65.

Pen, U.-L., Chang, T.-C., Hirata, C. M., and Peterson (2009). The GMRT EoR experiment: limits on polarized sky brightness at 150 MHz. *Monthly Notices of the Royal Astronomical Society*, 399(1):181–194.

Pritchard, J. R. and Furlanetto, S. R. (2006). Descending from on high: Lyman-series cascades and spin-kinetic temperature coupling in the 21-cm line. *Monthly Notices of the Royal Astronomical Society*, 367(3):1057–1066.

Pritchard, J. R. and Furlanetto, S. R. (2007). 21-cm fluctuations from inhomogeneous x-ray heating before reionization. *Monthly Notices of the Royal Astronomical Society*, 376(4):1680–1694.

Pritchard, J. R. and Loeb, A. (2012). 21 cm cosmology in the 21st century. *Reports on Progress in Physics*, 75(8):086901.

Robertson, B. E., Ellis, R. S., Dunlop, J. S., McLure, R. J., and Stark, D. P. (2010). Early star-forming galaxies and the reionization of the Universe. , 468(7320):49–55.

Rybicki, G. B. (2006). Improved fokker-planck equation for resonance-line scattering. *The Astrophysical Journal*, 647(1):709–718.

Seager, S., Sasselov, D. D., and Scott, D. (1999). A new calculation of the recombination epoch. *The Astrophysical Journal*, 523(1):L1–L5.

Thomas, R. M. and Zaroubi, S. (2008). Time-evolution of ionization and heating around first stars and miniqsos. , 384(3):1080–1096.

Tiltec (2022). Hydrogen line — Wikipedia, the free encyclopedia.

Wouthuysen, S. A. (1952). On the excitation mechanism of the 21-cm (radio-frequency) interstellar hydrogen emission line. , 57:31–32.

Zwart, J., Wall, J., Karim, A., Jackson, C., and Norris (2015). Astronomy Below the Survey Threshold in the SKA Era. In *Advancing Astrophysics with the Square Kilometre Array (AASKA14)*, page 172.